

Hydrodynamic couplings of colloidal ellipsoids diffusing in channels

Zhongyu Zheng^{1,2}, Xinliang Xu³, Yuren Wang^{1,2} and Yilong Han^{4,5,†}

¹Institute of Mechanics, Chinese Academy of Sciences, Beijing 100190, China

²School of Engineering Science, University of Chinese Academy of Sciences, Beijing 100049, China

³Beijing Computational Science Research Center, Beijing 100193, China

⁴Department of Physics, The Hong Kong University of Science and Technology, Hong Kong, China

⁵The Hong Kong University of Science and Technology, Shenzhen Research Institute, Shenzhen 518057, China

(Received 28 October 2020; revised 14 October 2021; accepted 18 November 2021)

The hydrodynamic interactions (HIs) of two colloidal spheres characterized by the translation–translation (T–T) couplings have been studied under various confinements, but little is known regarding the HIs of anisotropic particles and rotational motions, which are common in nature and industry. Here, we study the T–T, rotation–rotation (R–R) and translation–rotation (T–R) hydrodynamic couplings of two colloidal ellipsoids sediment on the bottoms of channels in experiment, theory and simulation. We find that the degree of confinement and the particle shape anisotropy are critical tuning factors resulting in anomalous hydrodynamic and diffusive behaviours. The negative R–R coupling reflects the tendency of opposite rotations of two neighbouring ellipsoids. The positive T–R coupling reflects that an ellipsoid rotates away from the channel axis as another ellipsoid approaches. As the channel width increases, the positive T–T coupling changes to an abnormal negative coupling, indicating that the single-file diffusion can exist even in wide channels. By contrast, only positive T–T couplings were observed for spheres in channels. The T–T coupling increases with the aspect ratio p . The R–R coupling is the maximum at a moderate $p \sim 2.8$. The T–R coupling is the maximum at a moderate degree of confinement. The spatial range of HIs is longer than that of spheres and increases with p . We propose a simple model which reproduces some coupling phenomena between two ellipsoids, and it is further confirmed by low-Reynolds-number hydrodynamic simulation. These findings shed new light on anisotropic particle diffusion in porous media, transport through membranes, microfluidics and microrheology.

Key words: colloids, Stokesian dynamics, microfluidics

† Email address for correspondence: yilong@ust.hk

1. Introduction

The motion of a particle in a fluid creates a local flow field which induces a drag force and torque on an adjacent particle and in turn on itself (Yang & Kim 1995). Such interparticle interactions mediated by the fluid, called hydrodynamic interactions (HIs), lead to the translation–translation (T–T), rotation–rotation (R–R) and translation–rotation (T–R) hydrodynamic couplings between particles (Happel & Brenner 1983). Hydrodynamic interactions depend on particles' size, shape and geometric confinement; they are of fundamental importance in fluid mechanics, with broad applications. For example, HIs play a critical role in the self- and collective diffusion (Dhont 1996), transportation (Doi & Edwards 1988), dynamic structure (Grzybowski, Stone & Whitesides 2000), rheological property (Foss & Brady 2000) and phase behaviours (Tanaka 2001, 2005). Colloids are important systems for the study of hydrodynamic couplings owing to their broad applications in soft matter, biophysics, chemical engineering, nanoscience and technology. The spontaneous random Brownian motions provide a statistical way to measure their coupled motions and HIs. Hydrodynamic interactions characterized by T–T couplings have been intensively studied for colloidal spheres in three dimensional (3D), quasi-two dimensional (q2D), and quasi-one dimensional (q1D) (Dufresne *et al.* 2000; Cui, Diamant & Lin 2002; Lin *et al.* 2002; Cui *et al.* 2004; Valley *et al.* 2007; Diamant 2009; Novikov *et al.* 2010; Misiunas *et al.* 2015) systems, but rarely for non-spherical particles and rotational motions in either unbounded or confined fluids.

In natural and industrial systems, however, most particles are non-spherical and their rotational motions and hydrodynamic torques are much more prominent than those of spheres. Particle's anisotropy and rotation strongly affect HIs resulting in rich behaviours of dynamics, structures, phases, rheology and self-assembly (Somasi *et al.* 2002; Duggal & Pasquali 2006; Han *et al.* 2006; Sokolov *et al.* 2007; Han *et al.* 2009; Zheng & Han 2010; Zheng, Wang & Han 2011; Zheng *et al.* 2014; Davidchack, Ouldrige & Tretyakov 2017). In addition, rotational motion and HIs are key factors in the cell–cell scattering (Drescher *et al.* 2011), bacterial swarming (Brotto *et al.* 2013; Dunkel *et al.* 2013), biofilm formation (Drescher *et al.* 2011; Mathijssen *et al.* 2016), feeding current in microorganism colonies (Grünbaum 1995) and pattern formation for fish-like swimmers (Dai *et al.* 2018). Despite its importance, HIs between two anisotropic particles are challenging to measure because they depend on not only particles' separation but also their orientations. Thus, two anisotropic particles have many more configurations than two spheres, and the statistics at each configuration is not enough for HI measurements. Hydrodynamic interactions for anisotropic particles have only been experimentally measured only in a few special cases, e.g. the longitudinal T–T coupling between two parallel aligned thin microrods trapped by optical tweezers (Di Leonardo *et al.* 2011) and the T–T couplings between a sphere and a dimer confined between two glass plates (Villanueva-Valencia *et al.* 2018). On the other hand, the rotational motion is difficult to detect experimentally for spherical particles. Rotational couplings were only theoretically studied between two spheres trapped in harmonic potentials with respect to both their positions and orientations in three-dimensional unbounded fluids (Reichert & Stark 2004) and experimentally tested for the temporal T–R coupling of two colloidal spheres in a special tangential relative motion (Martin *et al.* 2006). Theoretical and simulation studies usually apply simplified models and approximations inducing different levels of discrepancy with experiments (Cui *et al.* 2002; Misiunas *et al.* 2015). The accurate prediction of HIs for anisotropic particles, confined boundaries or rotational motions is much more difficult and complicated because the simplest spherical symmetry and point sphere approximation are no longer valid. Increasingly sophisticated methods have been developed to model suspension of

non-spherical particles by constructing mobility matrix for many particles (Mazur & van Saarloos 1982; Ladd 1994a,b; Berlyand & Panchenko 2007; Domínguez 2018), but the required hydrodynamic mobility tensor is an input parameter in prior. Here, we employ narrow channel confinement to reduce the possible configurations and perform long time observations to obtain good statistics for all the T–T, T–R and R–R couplings between two anisotropic particles.

Particle diffusions in geometric confinements are omnipresent in industrial and natural processes of chemistry, nanotechnology, geology and biology. Channel confinement is important in a wide range of problems from the transport of ions and proteins through biomembranes and porous media (Cacciuto & Luijten 2006; Usta, Butler & Ladd 2007) to the microfluidic applications in flow cytometry (Huh *et al.* 2005), bioassays (Huang *et al.* 2007), drug delivery (Pagès, James & Winterhalter 2008) and lab-on-a-chip (Stroock *et al.* 2000). Furthermore, a q1D channel leads to a single-file diffusion with non-trivial correlations and intriguing behaviours qualitatively different from the normal diffusions in two dimensions and three dimensions because particles cannot pass one another in q1D (Pozrikidis 1992; Wei, Bechinger & Leiderer 2000; Cui *et al.* 2002; Misiunas *et al.* 2015). Single-file diffusion in q1D channels has been intensively studied in experiments (Cui *et al.* 2002; Lin *et al.* 2002; Valley *et al.* 2007; Diamant 2009; Novikov *et al.* 2010; Misiunas *et al.* 2015), which are all about the translational motion and T–T HIs of spherical particles. It has been found that a q2D or q1D confinement can strongly affect the HIs of colloidal spheres: the T–T hydrodynamic coupling is long-ranged and decays with interparticle distance X as $1/X$ in an unbounded three-dimensional fluid (Happel & Brenner 1983) and near to a single wall (Blake 1971; Dufresne *et al.* 2000), and $1/X^2$ between two walls (Cui *et al.* 2004), but decays rapidly in q1D confinements to nearly zero in an upper-side-open long groove (Cui *et al.* 2002; Valley *et al.* 2007; Diamant 2009; Novikov *et al.* 2010) and a one-closed-ended short tube (Misiunas *et al.* 2015) or decays to a finite value in an open-ended tube (Misiunas *et al.* 2015). By contrast, little is known about the confinement effect on the HIs and single-file diffusion of anisotropic particles.

In this work, we present experimental measurements, theoretical modelling and numerical simulations of the T–T, R–R and R–T HIs between two anisotropic particles in channels for the first time, which all give consistent results. We directly measure the coupling diffusivities of colloidal ellipsoids freely diffusing in long-groove channels by fluorescent video microscopy. We explore the effects of particle anisotropy and degree of confinement on HIs by varying the ellipsoids' aspect ratio and the channel width; in fact, the effect of degree of channel confinement has not even been studied for spherical particles. Distinct HIs are discovered in different parameter regimes. We propose a simplified dumbbell-in-cylinder model that describes the experimental results remarkably well by fitting the dumbbell length and cylinder radius in different experimental parameter regimes, and further perform finite element numerical simulations to validate the model by quantitatively comparing with the experimental and theoretical results. Finally, we interpret the observed HIs and diffusion phenomena from the flow fields calculated in simulations. Because the colloidal particles are heavy enough to suppress out-of-plane fluctuations (similar to Cui *et al.* (2002), Valley *et al.* (2007) and Novikov *et al.* (2010)), the translational and rotational motions of the colloidal ellipsoids are measured in the x – y plane, i.e. quasi-2D, which is different from the scenarios of suspended particles that permit three-dimensional diffusion.

In theory and simulation, the calculation of HIs is difficult in terms of balancing the computational cost (Ermak & McCammon 1978; Happel & Brenner 1983; Diamant 2009) and the accuracy (Brady & Bossis 1988; Karrila, Fuentes & Kim 1989; Tran & Phan 1989).

The hydrodynamic coupling diffusivities, characterized by the off-diagonal terms of the diffusion tensors in diffusion matrix

$$\mathbf{D} = \begin{pmatrix} \mathbf{D}^{xx} & \mathbf{D}^{x\theta} \\ \mathbf{D}^{\theta x} & \mathbf{D}^{\theta\theta} \end{pmatrix}, \quad (1.1)$$

are usually obtained from a generalized Einstein relation (Montgomery & Berne 1977; Mazo 2002)

$$\mathbf{D} = k_{\text{B}} T \boldsymbol{\zeta}^{-1}. \quad (1.2)$$

The friction matrix $\boldsymbol{\zeta} = \begin{pmatrix} \zeta^{xx} & \zeta^{x\theta} \\ \zeta^{\theta x} & \zeta^{\theta\theta} \end{pmatrix}$ can be calculated through

$$\begin{pmatrix} \mathbf{F} \\ \mathbf{L} \end{pmatrix} = \boldsymbol{\zeta} \cdot \begin{pmatrix} \mathbf{u} \\ \boldsymbol{\omega} \end{pmatrix}, \quad (1.3)$$

by measuring the total hydrodynamic forces \mathbf{F} and torques \mathbf{L} imposing on a particle pair at the translational and rotational velocities $\mathbf{u} = \begin{pmatrix} u_1 \\ u_2 \end{pmatrix}$ and $\boldsymbol{\omega} = \begin{pmatrix} \omega_1 \\ \omega_2 \end{pmatrix}$. The diagonal or off-diagonal terms in each friction tensor of $\boldsymbol{\zeta}$ offer a velocity-independent measure of the hydrodynamic drag force (or torque) on a particle exerted by the flow field induced by its own or the other particle's movement, respectively (Montgomery & Berne 1977; Mazo 2002). Equation (1.2) reflects the fluctuation–dissipation relation which holds under thermal equilibrium. For three-dimensional motions, the superscripts, x, θ in (1.1)–(1.3) (see figure 1*a,b*) can also be replaced by y, z or ϕ . Previous studies only focused on the x – x and y – y couplings of colloidal spheres (Meiners & Quake 1999; Dufresne *et al.* 2000; Cui *et al.* 2002, 2004; Valley *et al.* 2007; Diamant 2009; Novikov *et al.* 2010; Misiunas *et al.* 2015) and here we study the x – x , x – θ , θ – θ , y – y , y – θ couplings, because the heavy colloidal spheres and ellipsoids barely fluctuate in the z direction. It provides a way to obtain $\boldsymbol{\zeta}$ by measuring \mathbf{D} from the random thermal displacements as used in the present experiment and previous colloid experiments about HIs (Meiners & Quake 1999; Dufresne *et al.* 2000; Cui *et al.* 2002, 2004; Lin *et al.* 2002; Martin *et al.* 2006; Valley *et al.* 2007; Novikov *et al.* 2010; Misiunas *et al.* 2015). Alternatively, $\boldsymbol{\zeta}$ can be directly calculated from its definition of (1.3) by measuring the force and the corresponding velocity without random thermal motions, as used in the present simulation (i.e. numerical solution), previous numerical simulation (Misiunas *et al.* 2015) and theory (Reichert & Stark 2004) about HIs. The total hydrodynamic force and torque can be represented by the integral of the force distribution density over the particle surface (Durlofsky, Brady & Bossis 1987; Ladd 1994*a,b*; Lisicki, Cichocki & Wajnryb 2016). Higher precision in the hydrodynamic description can be achieved by discretizing the particle surface finer and smoother at the expense of a higher computational cost. Various simplification and approximation methods are resorted to in an attempt to reduce the calculation expense and make the computation tractable, such as the finite element method (Misiunas *et al.* 2015; Villanueva-Valencia *et al.* 2018; Di Leonardo *et al.* 2011), the boundary element method (Palanisamy & den Otter 2018), the bead model (García de la Torre *et al.* 2007; Wajnryb *et al.* 2013; Lisicki *et al.* 2016), the lattice-Boltzmann model (Ladd 1994*a,b*), the raspberry swimmer model (de Graaf 2016) and the Oseen or Rotne–Prager approximation (Lin *et al.* 2002; Wajnryb *et al.* 2013; Bleibel *et al.* 2014; Goddard, Nold & Kalliadasis 2016; Palanisamy & den Otter 2018). Our theoretical model is in the spirit of the Stokeslet object model which is a recently developed promising method because it enables the simplest form to extract the geometric properties governing the HIs of arbitrarily shaped particles (Goldfriend, Diamant & Witten 2015;

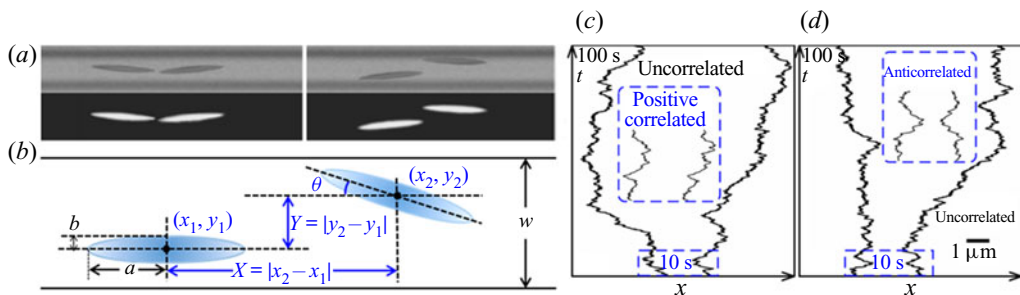


Figure 1. Coaxial ($Y/w \in [0, 0.1)$) and off-axis ($Y/w \in [0.5, 0.7)$) ellipsoid pairs in the q1D channel. (a) Bright field (upper) and fluorescent (lower) microscopy images of the coaxial (left) and off-axis (right) ellipsoid pairs. (b) Schematic diagram of sample geometry and ellipsoid separation. (c,d) Axial trajectories $x(t)$ (shifted 10 μm closer for clarity) of the coaxial (c) and off-axis (d) ellipsoid pairs; Insets are zoom-in views of the 10 s trajectories in the blue dashed boxes when X is less than the screening length X_{SC} . Aspect ratio $p = 7.5$ and channel width $w = 6 \mu\text{m}$.

Mowitz & Witten 2017; Witten & Mowitz 2019; Braverman, Mowitz, & Witten 2020; Witten & Diamant 2020). In this method, the object consists of a discrete set of points approximated as Stokeslets and separated by rigid distances, and the accuracy largely depends on the design of Stokeslets' configuration (Goldfriend *et al.* 2015; Mowitz & Witten 2017; Witten & Mowitz 2019; Braverman *et al.* 2020; Witten & Diamant 2020). Our findings indicate that the complex groove-like channels with different cross-sections can be simplified by cylindrical tubes and the Stokeslet approximation can well capture the hydrodynamic features of colloidal ellipsoids.

The remainder of the paper is organized as follows. We first describe the experimental system and the parameters of different samples in § 2. Experimental results of the T–T, R–R and T–R hydrodynamic couplings and comparison with other experiments are presented in § 3. The aim of § 4 is to provide a simple theoretical model for experimental results. Section 4.1 presents the dumbbell-in-cylinder model. Section 4.2 compares the experimental results with the model. The aim of § 5 is to make a comprehensive connection between experimental results and the model by the finite element numerical simulations. Section 5.1 compares with the simulation, experimental and theoretical results and § 5.2 demonstrates the flow field induced by a moving ellipsoid in a cylinder, which qualitatively explains the experimental results and the theoretical prediction. Finally, the work is summarized and concluded in § 6. Discussions and comparisons between the experimental, theoretical and numerical results can be found in §§ 5.1, 5.2 and 6.

2. Experimental systems

The sample cell comprised a polydimethylsiloxane (PDMS) substrate with long straight microgrooves and a glass slide. The substrate and slide were separated by two 100 μm -thick spacers. First, we placed a droplet of aqueous suspension of colloidal ellipsoids onto the glass slide. The dilute colloidal suspension was absorbed into the sample cell due to the capillary force. Then, we quickly sealed the sample cell with epoxy glue. After approximately 30 min, the colloidal ellipsoids sediment onto the bottom of the microgrooves in the PDMS substrates. Finally, the Brownian motions of the colloidal ellipsoids in the grooves were observed under an optical microscope and recorded using a charge-coupled device camera at 10 frames per second (see figure 1a). The centre-of-mass (CM) positions (x, y) and orientations θ of individual ellipsoids (see figure 1b) were

tracked according to our image processing algorithm with an angular resolution of 1° and spatial resolutions of 0.07 and 0.04 μm along the long and short axes, respectively (Zheng & Han 2010).

To make the microgrooves, we fabricated lines of photoresist with widths of $w = 4, 5$ and 6 μm ; a height of $d = 5 \mu\text{m}$; and a length of $l = 1 \text{ cm}$ on a silicon wafer through photolithography. Subsequently, the line patterns of the photoresist mask were printed on the PDMS substrate using soft lithography to form upper-side-open microgrooves with rectangular cross-sections and the same w, d and l . The PDMS rectangular grooves have sharp corner edge and $< 100 \text{ nm}$ surface roughness on the upper surface and bottom.

In bright-field microscopy, the position of an ellipsoid cannot be very accurately measured due to the interference from the nearby channel edges. To accurately track the ellipsoids, we fabricated ellipsoids by stretching fluorescent spheres (Han *et al.* 2009; Zheng & Han 2010) and imaged the ellipsoids under fluorescent microscopy (see figure 1*a*). Briefly, we added 3.26 μm -diameter fluorescent polystyrene (PS) spheres (0.5% by weight) into an aqueous solution of polyvinyl alcohol (PVA) (12% by weight) in a Petri dish, and heated and stretched the solid PVA film after water evaporation. The PS spheres embedded in the PVA film were stretched into ellipsoids at 110°C , which is above the glass transition temperatures of PVA ($T_g = 85^\circ\text{C}$) and PS ($T_g = 90^\circ\text{C}$). After cooling to room temperature, the PVA was dissolved and washed away with deionized water several times. We fabricated five batches of ellipsoids with aspect ratios $p = a/b = 1.8, 2.2, 2.8, 5.2$ and 7.5 , where a and b were the semimajor and semiminor axes, respectively. The polydispersity of p was carefully controlled to less than 3%. The size ratios between the ellipsoids and the channel widths were chosen to enable quantitative exploration of the effects of particle anisotropies and degree of channel confinement on HIs, and to limit the particles' orientational degrees of freedom to a small range by the narrow channel confinement. Next, 7 mM sodium dodecyl sulphate was added to stabilize the suspension (Zheng & Han 2010). The pair potential between two ellipsoids was calculated from $U(X) = -k_B T \ln g(X)$ according to the Boltzmann distribution at a low density where the multibody effect is negligible. Here, X is the CM separation along the axial direction (see figure 1*b*); and the one-dimensional radial distribution function, $g(X) = \langle \sum_{i \neq 0} \delta(x - x_i) \rangle / \rho$, was directly measured from the histogram of X normalized by the linear density $\rho = N/l$, where N is the total number of particles in the channel length l . The colloidal ellipsoids showed a hard-core pair potential, indicating that they can be regarded as hard particles without attractions or repulsions. According to the Boltzmann distribution, ellipsoids exhibit an exponential distribution along the z direction with a characteristic length of the gravitational height $h = k_B T / (mg) = 0.424 \mu\text{m}$, where mg is the buoyancy weight of the ellipsoid. Here, h is much smaller than the particle size, indicating that the ellipsoids are heavy enough to sediment to the bottom of the channel with little fluctuations in the z direction. Such small distance between the particle and the bottom surface dominates particles' drags, but does not qualitatively change HIs. It confines the angle fluctuation to merely 2° – 5° for ellipsoids with aspect ratios ranging from 7.5 to 1.8. This is confirmed by the observation that ellipsoids' centres and tips barely fluctuate out of the focal plane, i.e. the fluctuation is less than the 0.4 μm focal depth of the microscope objective.

The HIs were measured as functions of the particle CM separation (X, Y) (see figure 1*b*) with sufficient statistics for accurate measurements in different parameter regimes ($p, w, Y/w$) via very long ($> 24 \text{ h}$) observations for each sample with a certain p and w . The linear packing fraction $\phi = 2aN/l$ was moderately low ($0.05 \leq \phi \leq 0.3$) to form many isolated ellipsoid pairs in channels; that is, other ellipsoids were more than $10a$ away and had little effect due to the short-range nature of HIs in the narrow grooves. In a

long video of an equilibrium q1D dilute gas, all the video sections with isolated ellipsoid pairs (i.e. $X < 10a$ and other particles $> 10a$ away) are used for HI measurements. Both approaching and receding motions of two ellipsoids are observed.

3. Experimental results

3.1. The x - x , x - θ , θ - θ , coupling diffusivities

The HIs of ellipsoid pairs are characterized by the x - x , θ - θ and x - θ coupling diffusivities, as follows:

$$\begin{cases} D_C^{xx} = \langle \Delta x_1 \Delta x_2 \rangle / (2t), \\ D_C^{\theta\theta} = \langle \Delta \theta_1 \Delta \theta_2 \rangle / (2t), \\ D_C^{x\theta} = \langle \Delta x_1 | \Delta \theta_2 \rangle / (2t) = -\langle | \Delta \theta_1 | \Delta x_2 \rangle / (2t) = -D_C^{\theta x}, \end{cases} \quad (3.1)$$

where Δx_i is the CM displacement along the channel axis, and $\Delta \theta_i$ is the angular displacement with $-\pi/2 \leq \theta \leq \pi/2$ of ellipsoid i during time interval t (see figure 1b). Here $\langle \rangle$ is an average over trajectories of all isolated pairs at all times from experimental trials. The first equation in (3.1) has been used in previous studies about colloidal spheres (Cui *et al.* 2002, 2004; Mazo 2002; Valley *et al.* 2007; Diamant 2009; Novikov *et al.* 2010), but the latter two about rotational motions have not been applied to colloidal experiments. In the diffusion matrix (Montgomery & Berne 1977; Mazo 2002) $D(X, Y)$ (see (1.1)), D_C^{xx} , $D_C^{\theta\theta}$ and $D_C^{x\theta}$ are the off-diagonal terms of the diffusion tensors D^{xx} , $D^{x\theta}$, and $D^{\theta\theta}$, while the diagonal terms are the self-diffusivities $D_S^{xx} \equiv \langle \Delta x_1^2 \rangle / (2t)$, $D_S^{\theta\theta} \equiv \langle \Delta \theta_1^2 \rangle / (2t)$ and $D_S^{x\theta} \equiv \langle \Delta x_1 \Delta \theta_1 \rangle / (2t)$.

The experimental results of $D_C^{xx}(X)$, $D_C^{\theta\theta}(X)$ and $D_C^{x\theta}(X)$ at different degrees of off-axial distance Y/w are shown in figure 2 for different p and in figure 3 for different w . The effects of $(w, Y/w)$ have not been explored even for T-T HIs of two spheres. In our experiment, they all show strong couplings at small X which decay with increasing X and vanish beyond X_{SC} , reflecting a screening effect of the channel confinement on the HIs. The screening length X_{SC} is defined as the minimal X where $|D_C(X)| \leq 0.1|D_C(X)|_{MAX}$. The screening of HIs results in uncorrelated axial trajectories of ellipsoid pairs at $X > X_{SC}$ (see figure 1c,d). Interestingly, we find that D_C^{xx} changes sign as Y/w increases: $D_C^{xx} > 0$ at $Y/w < 0.5$ and $X < X_{SC}$ for various p (see figure 2a-c) and various w (see figure 3a-c), whereas $D_C^{xx} < 0$ at $Y/w > 0.5$ (see figures 2d and 3d). Such positive and negative x - x couplings are directly observed from the concerted single-file movements of ellipsoid pairs that are in the same directions at $Y/w < 0.1$ (see inset of figure 1c) but in opposite directions at $Y/w > 0.5$ (see inset of figure 1d). We emphasize that the positive axial HI ($D_C^{xx} > 0$) dominates in q1D confinements with $w/b < 4$ which is too strong to allow particles passing each other, while the anomalous negative axial HI ($D_C^{xx} < 0$) occurs in weak channel confinement ($w/b > 4$). By contrast, for spherical particles in q1D or wide channels, only positive x - x couplings were observed (Cui *et al.* 2002; Lin *et al.* 2002; Novikov *et al.* 2010; Misiunas *et al.* 2015). It is well known that the single-file movements of the spheres occurred only in q1D confinements (Cui *et al.* 2002; Lin *et al.* 2002; Misiunas *et al.* 2015). By contrast, our result shows that single-file diffusions of ellipsoids can occur in wide channels because two off-axis ellipsoids tend to separate apart ($D_C^{xx} < 0$) when they get close to each other.

The θ - θ coupling is negative ($D_C^{\theta\theta} < 0$) at $X < X_{SC}$ for various p , w and Y/w (see figures 2e-h and 3e-h), indicating that an ellipsoid's clockwise rotation tends to induce its neighbour's anticlockwise rotation. The x - θ coupling is positive ($D_C^{x\theta} > 0$)

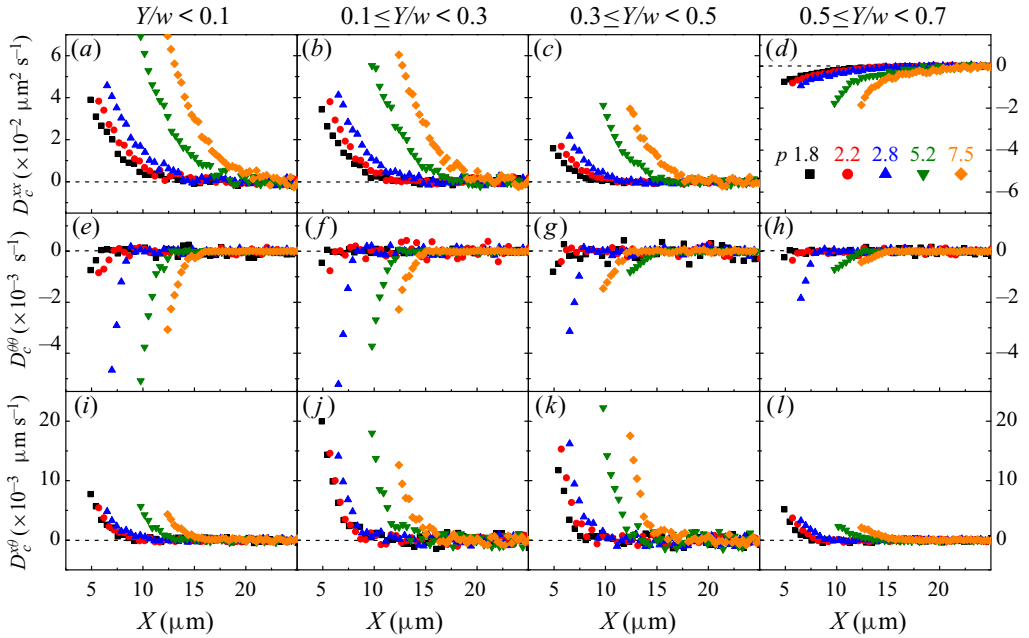


Figure 2. The experimental coupling diffusivities of ellipsoid pairs with different aspect ratio p as functions of interparticle distance (X, Y) in a channel of width $w = 6 \mu\text{m}$. Here (a–d) D_C^{xx} , (e–h) $D_C^{\theta\theta}$ and (i–l) $D_C^{x\theta}$. The transverse interparticle separation $Y/w \in [0, 0.1)$, $[0.1, 0.3)$, $[0.3, 0.5)$ and $[0.5, 0.7)$ in (a,e,i), (b,f,j), (c,g,k) and (d,h,l), respectively.

(see figures 2i–l and 3i–l), indicating that an ellipsoid tends to rotate away from the channel axis as a neighbour approaches, and *vice versa*.

The screening lengths measured from figures 2 and 3 for various p and w are shown in figure 4. We find that X_{SC} linearly increases with the long axis of ellipsoids (see figure 4a), leading to a rapid amplification of X_{SC} with particles' shape anisotropy. For the same p , X_{SC} slowly increases with w (see figure 4b), reflecting a slightly stronger screening of HIs in a narrower channel. These results indicate that X_{SC} is much more sensitive to the particle elongation than the channel width in upper-side-open groove channels. By contrast, X_{SC} is on the length scale of w for colloidal spheres in the upper-side-open groove channels (Lin *et al.* 2002; Valley *et al.* 2007). Therefore, particle elongation can extend the effective range of HIs exceeding the channel width ($X_{SC} \gg w$) as shown in figure 4(b). In addition, we find that X_{SC}/a is the largest for D_C^{xx} and the smallest for $D_C^{\theta\theta}$, indicating a stronger suppression of rotational HIs than axial translational HIs by the channel confinement. Particles at different Y/w have similar behaviours of X_{SC} .

The HIs can also be characterized by the Pearson correlation coefficient (Misiunas *et al.* 2015): $\rho^{xx} \equiv \text{cov}(\Delta x_1, \Delta x_2)/(\sigma(\Delta x_1)\sigma(\Delta x_2))$ and similarly defined $\rho^{\theta\theta}$ and $\rho^{x\theta}$, where cov is the covariance, σ is the standard deviation. They are equivalent to the normalized hydrodynamic coupling diffusivities $\rho^{xx} = D_C^{xx}/D_S^{xx}$, $\rho^{\theta\theta} = D_C^{\theta\theta}/D_S^{\theta\theta}$ and $\rho^{x\theta} = D_C^{x\theta}/(D_S^{xx}D_S^{\theta\theta})^{1/2}$, which exclude the influence of channel confinement and particle anisotropy on self-diffusivities and enable a more precise comparison of HIs in different regimes of parameters ($p, w, Y/w$) (Riley, Hobson & Bence 2006; Misiunas *et al.* 2015). Figure 5 presents ρ^{xx} , $\rho^{\theta\theta}$ and $\rho^{x\theta}$ as functions of the tip-to-tip distance of the ellipsoid pair. For the same tip-to-tip distance, the absolute value $|\rho^{xx}|$ increases more than one time

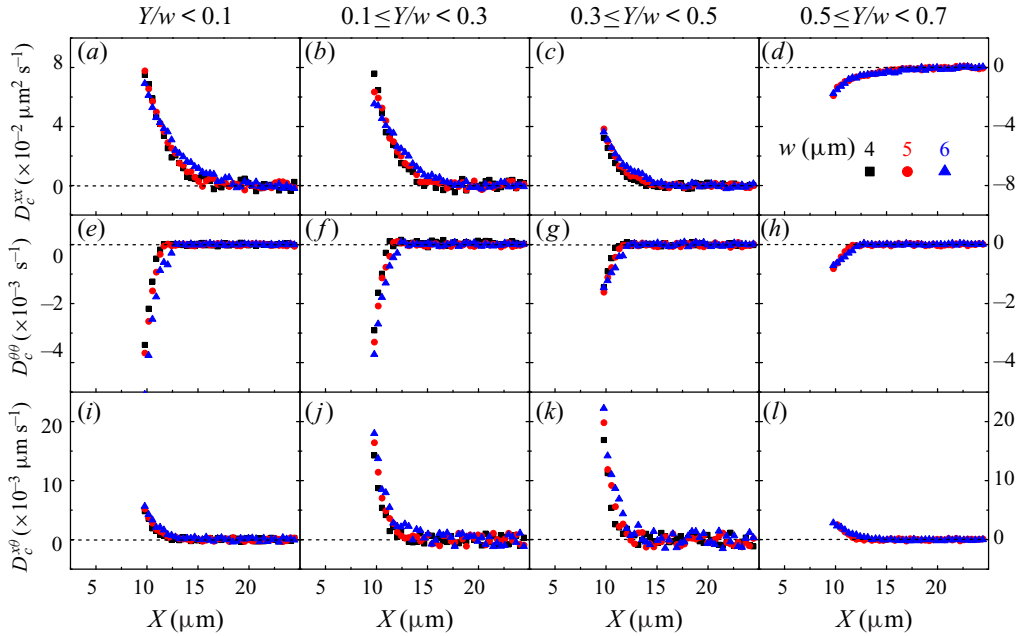


Figure 3. The experimental results of coupling diffusivities of ellipsoid pairs of aspect ratio $p=5.2$ as functions of interparticle separation (X, Y) in channels of different width w . Here (a–d) D_C^{xx} , (e–h) $D_C^{\theta\theta}$ and (i–l) $D_C^{x\theta}$. The transverse interparticle separation $Y/w \in [0, 0.1)$, $[0.1, 0.3)$, $[0.3, 0.5)$ and $[0.5, 0.7)$ in (a,e,i), (b,f,j), (c,g,k) and (d,h,l), respectively.

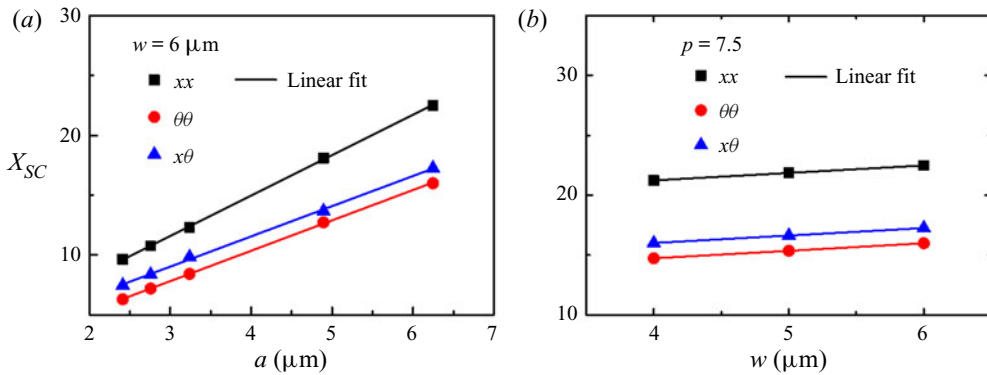


Figure 4. The screening lengths X_{SC} (symbols) for D_C^{xx} , $D_C^{\theta\theta}$ and $D_C^{x\theta}$ of the coaxial ellipsoid pairs ($Y/w \in [0, 0.1)$). Here (a) X_{SC} for different p and $w=6 \mu\text{m}$ and (b) X_{SC} for different w and $p=7.5$. The lines are linear fittings.

as p increasing from 1.8 to 7.5 (see figure 5a–d), reflecting an enhanced T–T HIs for more anisotropic particles. Here $|\rho^{\theta\theta}|$ is non-monotonic with p and reaches the maximum at $p = 2.8$ (see figure 5e–h), reflecting the strongest R–R HIs at medium aspect ratios. We attribute the weak R–R HI as the small torque of the short moment arm for small p and the suppression from the channel confinement for large p . Here $|\rho^{xx}|$ and $|\rho^{\theta\theta}|$ decrease at larger Y/w , reflecting the suppression of T–T and R–R HIs for off-axis particle pairs which are closer to the channel walls. By contrast, figure 5(i–l) show that the maximum $\rho^{x\theta}$

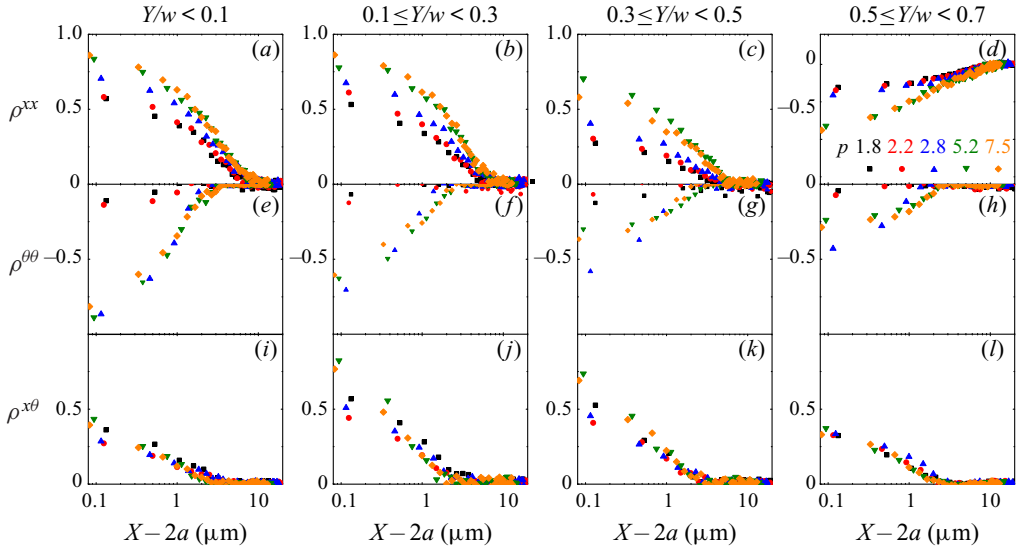


Figure 5. The Pearson correlation coefficients of coupling diffusivities of ellipsoid pairs as functions of the interparticle tip-to-tip distance ($X - 2a, Y$) in a channel of width $w = 6 \mu\text{m}$. Here (a–d) ρ^{xx} , (e–h) $\rho^{\theta\theta}$ and (i–l) $\rho^{x\theta}$. The transverse interparticle separations $Y/w \in [0, 0.1]$, $[0.1, 0.3]$, $[0.3, 0.5]$ and $[0.5, 0.7]$ in (a,e,i), (b,f,j), (c,g,k) and (d,h,l), respectively.

appears at middle Y/w , reflecting the strongest T–R HIs for moderate off-axis particles. The non-monotonic changes of $\rho^{\theta\theta}$ with p (see figure 5e–h) and $\rho^{x\theta}$ with Y/w (see figure 5i–l) reflect non-trivial θ – θ and x – θ couplings. We explain these experimental results based on a theoretical model and low-Reynolds-number numerical simulation in the following sections.

3.2. The y–y and y– θ coupling diffusivities

We next measure HIs about the transverse displacements by the y–y and y– θ coupling diffusivities as functions of (X, Y): $D_C^{yy} = \langle \Delta y_1 \Delta y_2 \rangle / (2t)$ and $D_C^{y\theta} = \langle \Delta y_1 \Delta \theta_2 \rangle / (2t) = \langle \Delta \theta_1 \Delta y_2 \rangle / (2t) = D_C^{\theta y}$ in figure 6, where Δy_i is the CM displacement of ellipsoid i in the transverse direction of the channel during time interval t . Here $D_C^{xx}(X)$ and $D_C^{yy}(X)$ of two spheres have been measured in three dimensions (Meiners & Quake 1999) and quasi-two dimensions (Cui *et al.* 2004; Valley *et al.* 2007; Diamant 2009). In the present study, we comprehensively measure $D_C^{xx}, D_C^{\theta\theta}, D_C^{x\theta}, D_C^{yy}$ and $D_C^{y\theta}$ for ellipsoid pairs as a function of X and Y (see figures 2, 3 and 6).

Figure 6 shows that $D_C^{yy}(X)$ and $D_C^{y\theta}(X)$ are nearly zero for different p and Y/w , reflecting vanishing y–y and y– θ couplings. This is attributed to the strong suppression of transverse motion in channel confinement as shown from the very small fluctuations in the transverse trajectories of ellipsoids (see figure 7a). In addition, we observe that two neighbouring ellipsoids with $2a < X < X_{SC}$ tend to locate symmetrically in the transverse direction about the central axis ($y = 0$) of the channel, that is, $y_1(t) = -y_2(t)$ (see figures 1a,b and 7); and the isolated single ellipsoids tend to equilibrate on the central axis, that is, $|y(t)| < 0.05w$ (see figure 7a). Note that $X > 2a$ always hold since the ellipsoids cannot pass by each other in the narrow channel. Similar phenomena were observed in constant microfluidic

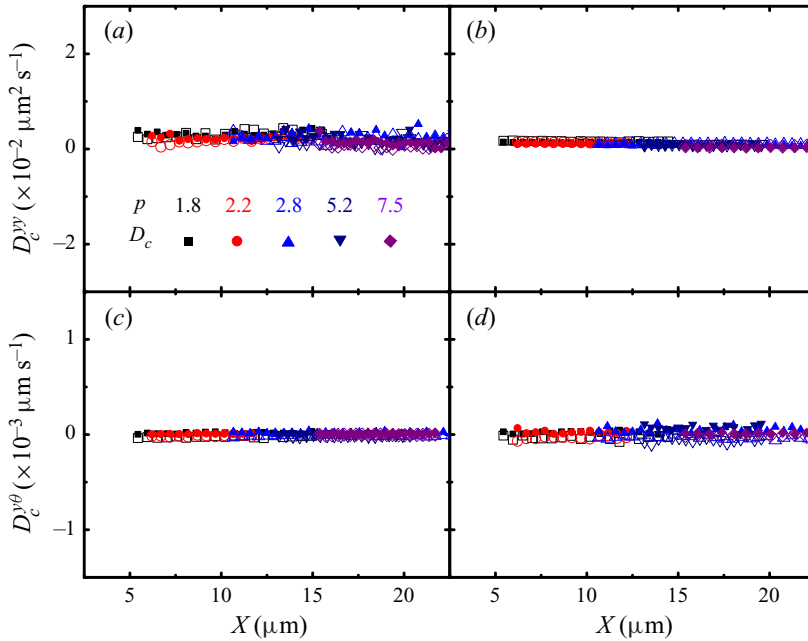


Figure 6. The experimental results of y - y and y - θ coupling diffusivities. Here (a,b) D_C^{yy} and (c,d) $D_C^{y\theta}$ indicate no hydrodynamic coupling. Ellipsoid pairs with different p and at different axial interparticle distance X in a channel of $w = 6 \mu\text{m}$. (a,c) Coaxial ($Y/w \in [0, 0.1)$) and (b,d) off-axis ($Y/w \in [0.5, 0.7)$) ellipsoid pairs.

flows in which the isolated polymers diffused towards the channel central axis (Usta, Ladd & Butler 2005) and the adjacent spherical droplets located symmetrically about the central axis and form zigzag patterns (Beatus, Tlusty, & Bar-Ziv 2006; Fleury *et al.* 2014). These phenomena have been interpreted as resulting from the dipolar flow field around each particle in the channel confinement (Uspal & Doyle 2014). However, the HIs and diffusion behaviours of particles due to the dipolar flow have not been measured. Our results indicate that the channel confinement suppresses the transverse motion much more than the rotational motion due to the large viscous drag along the ellipsoid short-axis. That is to say, the effect of the transverse component of a local dipolar flow created by a moving particle imposes a torque on the other particle and induces a rotational motion of that particle rather than a transverse motion.

4. Theoretical analysis

4.1. Dumbbell-in-cylinder model

The flow field created by a moving particle is usually estimated using the point force (Stokeslet) approximation (Batchelor 1970; Cui *et al.* 2002, 2004; Hernández-Ortiz, de Pablo & Graham 2006; Valley *et al.* 2007; Diamant 2009; Novikov *et al.* 2010). For example, a spherical particle, an elongated particle and a long-thin rod or fibre are often modelled as a point force (Cui *et al.* 2002, 2004; Valley *et al.* 2007; Diamant 2009; Novikov *et al.* 2010), a dumbbell of two point forces (Hernández-Ortiz *et al.* 2006; Bukowicki, Gruca, & Ekiel-Jezewska 2014) and a line of point forces (Batchelor 1970; Di Leonardo *et al.* 2011; de Graaf *et al.* 2016), respectively. The T-T hydrodynamic coupling of colloidal spheres has been described by treating the moving sphere as a point force

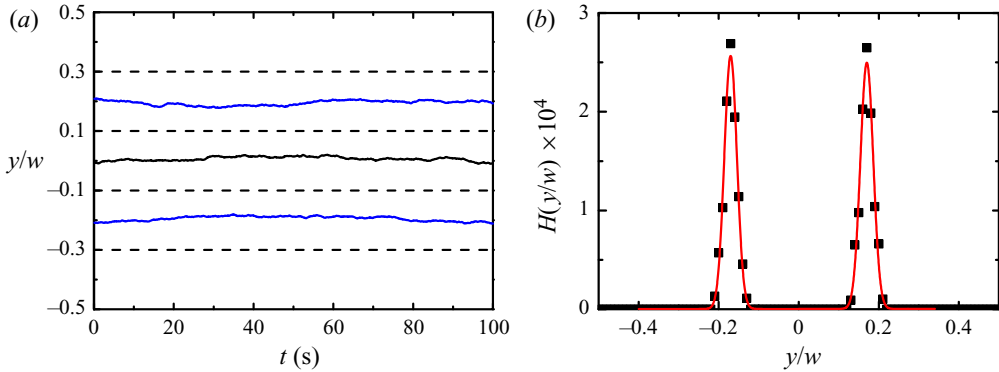


Figure 7. (a) Typical transverse positions $y(t)/w$ of an ellipsoid pair with $2a < X < X_{SC}$ (blue curves) and a single ellipsoid (black curve). The channel boundary is at $Y/w = \pm 0.5$. (b) The corresponding histogram of the transverse positions $H(y_1/w)$ and $H(y_2/w)$ of the ellipsoid pair with $2a < X < X_{SC}$ (symbols) and the Gaussian fits (curves). The aspect ratio $p = 7.5$, and the channel width $w = 6 \mu\text{m}$.

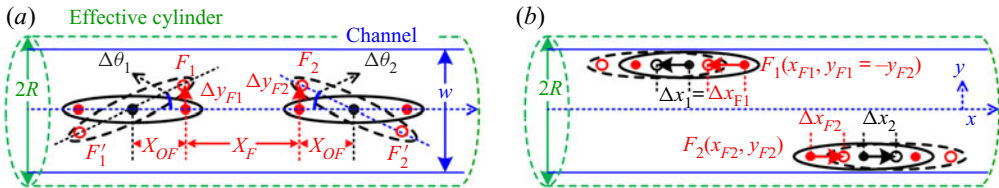


Figure 8. Schematic diagram of the dumbbell-in-cylinder model. (a) Rotational displacement $\Delta\theta$ and (b) axial displacement Δx of an ellipsoid pair between time $= 0$ (solid ellipses with filled circles) and time $= t$ (dashed ellipses with open circles) in the effective cylinder (green dashed contours) of diameter $2R$ which is equivalent to a channel (solid blue lines) of width w . The subscript represents ellipsoid 1 or 2. The dumbbell of point forces $F(x_F, y_F)$ and $F'(x_{F'}, y_{F'})$ at the red circles are symmetric about the ellipsoid's CM (black circle) at (x, y) along the long axis. The transverse force $F^y = -F'^y$ in (a) and axial force $F^x = F'^x$ in (b) are proportional to the translational and axial displacements (red arrows) $\Delta y_F = -\Delta y_{F'}$ and $\Delta x_F = \Delta x_{F'}$, respectively (Goldfried *et al.* 2015).

at the sphere centre (Cui *et al.* 2002, 2004; Valley *et al.* 2007; Diamant 2009; Novikov *et al.* 2010). The translation of a spheroid in unbounded flow has been described by a line distribution of Stokeslets between the foci (Chwang & Wu 1976). Here, we proposed a simplified dumbbell-in-cylinder model to estimate the T–T, R–R and T–R coupling of two ellipsoids in channels. This model is based on the following three approximations as illustrated in figure 8 and summarized in table 1. (i) The motion of an ellipsoid is treated as a dumbbell of point forces (F, F'), that is to say, the effect of the flow field induced by an ellipsoid on the other is equivalent to exerting (F, F') on the fluid. The dumbbell length is $2X_{OF}$ along the long axis with the centre coinciding with the ellipsoid's CM. (ii) The HIs between two ellipsoids are dominated by the point-force pair F_1 and F_2 near the centre of the two ellipsoids. Here F'_1 and F'_2 at the far ends can be neglected due to the strong screening of HIs in the channel. (iii) The confinement effect of a rectangular groove with an open side is equivalent to that of a cylinder with a radius $R > w$ as confirmed in Cui *et al.* (2002), Diamant (2009) and Novikov *et al.* (2010). These assumptions hold well under the low Reynolds number ($\sim 10^{-6}$), the no-slip boundary conditions (Happel & Brenner 1983), $b \ll R$, and $(a - X_{OF}) \ll X_F$.

According to this theoretical model, the T–T, T–R and R–R HIs between ellipsoids are treated as derived from the x – x , x – y and y – y components of the Stokeslet tensor.

System	Ellipsoid pair in experiment	Point-force pair in dumbbell-in-cylinder model
Parameters	a, b, w	X_{OF}, R
Coordinates	$(x_1, y_1, \theta_1), (x_2, y_2, \theta_2)$	$(x_{F1} = x_1 + X_{OF}, y_{F1} \approx y_1), (x_{F2} = x_2 - X_{OF}, y_{F2} \approx y_2)$
Separations	$X = x_1 - x_2 , Y = y_1 - y_2 = 2 y_1 $	$X_F = X - 2X_{OF}, Y_F \approx Y$
Displacements	$(\Delta x_1, \Delta \theta_1), (\Delta x_2, \Delta \theta_2)$	$(\Delta x_{F1} = \Delta x_1, \Delta y_{F1} \approx X_{OF} \Delta \theta_1), (\Delta x_{F2} = \Delta x_2, \Delta y_{F2} \approx -X_{OF} \Delta \theta_2)$
Coupling diffusivities	$D^{xx}(X, Y), D^{x\theta}(X, Y), D^{\theta\theta}(X, Y)$	$\Delta^{xx}(X_F/R, Y_F/R), \Delta^{xy}(X_F/R, Y_F/R), \Delta^{yy}(X_F/R, Y_F/R)$

Table 1. Summary of the parameters, coordinates and coupling diffusivities in the experiment and theoretical models with subscript 1 or 2 denoting the left or right ellipsoid in [figure 8](#).

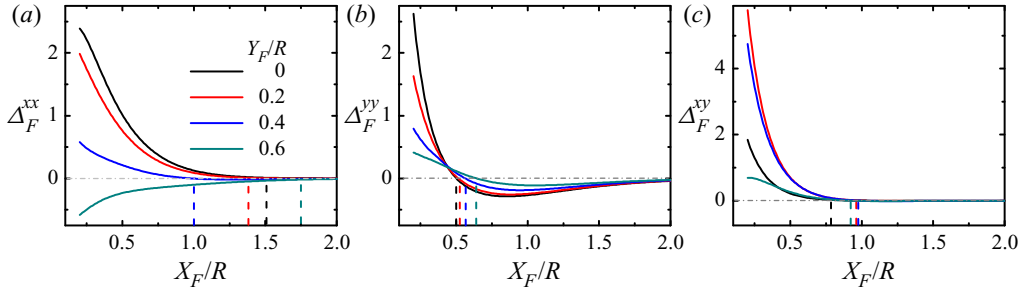


Figure 9. Theoretical estimates of the (a) x - x , (b) y - y and (c) x - y coupling diffusivities of point-force pairs as functions of the rescaled axial distance X_F/R and transverse distance Y_F/R calculated from (4.2).

The axial translational and rotational displacements $(\Delta x, \Delta \theta)$ of an ellipsoid can be represented by the axial and transverse displacements $(\Delta x_F, \Delta y_F)$ (see figure 8 and table 1). Consequently, $D_C(X, Y)$ of an ellipsoid pair in a channel can be approximately transformed into the dimensionless coupling diffusivities in an effective cylinder

$$\Delta_F^{\mu\nu} \equiv \langle \Delta \mu_{F1} \Delta \nu_{F2} \rangle / (2tk_B T / 6\pi\eta R), \quad (4.1)$$

as functions of the rescaled axial and transverse separations $X_F/R = (X - 2X_{OF})/R$ and $Y_F/R \approx Y/R$ (see figure 8 and table 1), where $\mu, \nu = x$ or y and η is the fluid viscosity. By substituting the Stokes-flow Oseen tensor in a cylinder derived from Liron & Shahar 1978 and Blake 1979 into (4.1), we obtained the theoretical equations

$$\begin{aligned} \Delta_F^{\mu\nu}(X_F/R, Y_F/R) = 6\pi^2 \sum_{k=0}^3 \sum_{n=1}^3 \{ & [a_{kn}^{\mu\nu}(Y_F/R) \cos(\alpha_{kn} \cdot X_F/R) \\ & + b_{kn}^{\mu\nu}(Y_F/R) \sin(\alpha_{kn} \cdot X_F/R)] e^{-\beta_{kn} \cdot (X_F/R)} \\ & + c_{kn}^{\mu\nu}(Y_F/R) e^{-\gamma_{kn} \cdot (X_F/R)} \}, \end{aligned} \quad (4.2)$$

where the values of $(\alpha_{kn}, \beta_{kn}, \gamma_{kn})$ and $(a_{kn}^{\mu\nu}, b_{kn}^{\mu\nu}, c_{kn}^{\mu\nu})$ can be obtained from Liron & Shahar (1978). Details about the theoretical expression are given in the Appendix (A). The theoretical results of $\Delta_F^{\mu\nu}$ at different $(X_F/R, Y_F/R)$ in the dumbbell-in-cylinder model are shown in figure 9.

4.2. Comparisons between the experimental and theoretical results

We quantitatively compare the experimental D_C with the theoretical prediction of the aforementioned model in figure 10. The two parameters X_{OF} and R in different $(p, w, Y/w)$ regimes can be fitted from two out of three couplings Δ_F^{xx} , Δ_F^{yy} and Δ_F^{xy} . For example, the fitted X_{OF} and R from Δ_F^{xx} , Δ_F^{yy} can describe Δ_F^{xy} well, and have no discernable difference from their best fits from all the three couplings, indicating that the dumbbell-in-cylinder model is effective. Moreover, figure 11(a) shows that R fitted at a certain $(w, Y/w)$ is robust at different p , indicating that R is a good parameter for describing the effects of the channel without the effects of ellipsoids. Figure 11(d) shows that X_{OF} at a certain p is robust at different $(w, Y/w)$, indicating that X_{OF} is a good parameter for describing the effects of particles without the effects of the channel. We find that the theoretical model can describe the experimental data well by taking only the leading terms. As depicted in

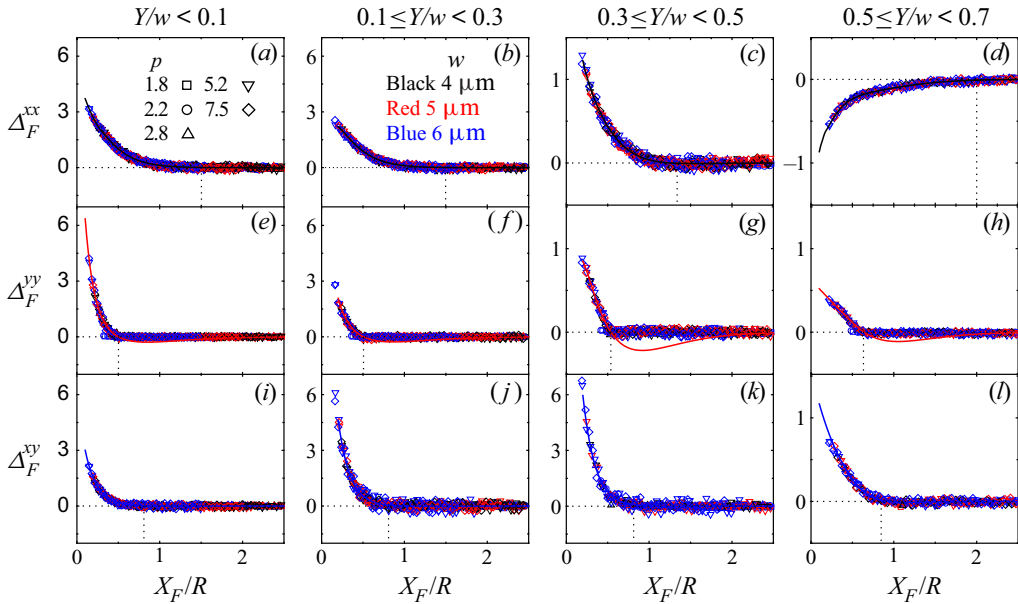


Figure 10. Rescaled coupling diffusivities (a–d) Δ_F^{xx} , (e–h) Δ_F^{yy} and (i–l) Δ_F^{xy} as functions of $\xi^x = X_F/R$. The experimental data (symbols) for all p and w collapse onto the theoretical fittings of (4.2) (solid curves) except for the negative part of Δ_F^{xx} . The transverse separation of the ellipsoid pairs $Y/w \in [0, 0.1)$, $[0.1, 0.3)$, $[0.3, 0.5)$ and $[0.5, 0.7)$ in (a,e,i), (b,f,j), (c,g,k) and (d,h,l), respectively, with the fitted $Y/R = 0.04, 0.14, 0.32$ and 0.52 . Vertical dashed lines mark the screening length X_{SC}^F .

figure 10, the experimental $\Delta_F(X_F/R)$ (symbols) for all p and w at each Y/w collapse onto the theoretical curves at the corresponding Y/R , suggesting a general mechanism of the Stokes-flow-induced hydrodynamic couplings. The experimental positive and negative x – x couplings of ellipsoid pairs at $Y/w < 0.5$ (see figures 2a–c and 3a–c) and $Y/w > 0.5$ (see figures 2d and 3d) are described well by the theoretical $\Delta_F^{xx} > 0$ at $Y_F/R < 0.5$ (see figure 10a–c) and $\Delta_F^{xx} < 0$ at $Y_F/R > 0.5$ (see figure 10d), respectively. The negative θ – θ (see figures 2e–h and 3e–h) and positive x – θ (see figures 2i–l and 3i–l) couplings of ellipsoid pairs agree with the theoretical $\Delta_F^{yy} > 0$ (see figure 10e–h) and $\Delta_F^{xy} > 0$ (see figure 10i–l). These consistent results reflect that the axial and transverse flows drive the axial and rotational motion of an ellipsoid, and T–T, R–R and T–R couplings reflect well the effect of HIs mediated by the x – x , y – y and x – y components of the induced flow. A reverse sign in Δ_F^{yy} at $X_F/R \sim 1.0$ is predicted to arise from the alternating signed eddies of the Stokeslet along the channel (Liron & Shahar 1978; Blake 1979), which is not observed experimentally here for ellipsoids nor for colloidal spheres previously (Novikov *et al.* 2010). This discrepancy probably occurs because the surface of ellipsoid 1 between the point force and the tip, i.e. in the range of $(x_1 + X_{OF}, x_1 + a)$ near ellipsoid 2, produces positive Δ_F^{yy} and *vice versa*, which superposes onto the negative Δ_F^{yy} when the interparticle distance is more than the screening distance ($X > X_{SC}$ in the experiment, i.e. $X_F > X_{SC}^F$ in the model). An accurate description needs an integration over the whole surface of the particle, see the finite element numerical simulations in § 5 which fully recover the experimental Δ_F^{yy} ; however, our dumbbell model approximates each ellipsoid only by one point force which can describe the average effect within the screening distance ($X_F < X_{SC}^F$).

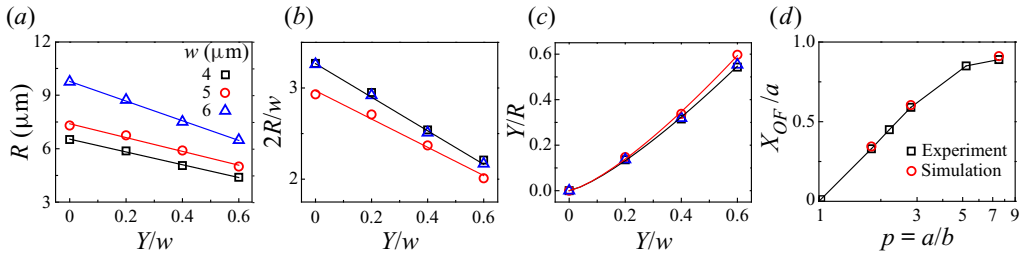


Figure 11. The effective cylinder radius R and semidumbbell length X_{OF} in the dumbbell-in-cylinder model. Here (a) R (symbols) versus Y/w obtained from figure 10 with linear fittings (solid lines) for experiments at different w and for all p ; (b) $2R/w$ versus Y/w rescaled from (a) with the linear fittings (solid lines); (c) Y/R versus Y/w rescaled from (a) with power-law fittings (solid curves), in (b,c), the black fitting curves are for square and triangle symbols; (d) X_{OF}/a versus p for experiment (black squares) obtained from figure 10 and for numerical simulation (red circles) fitted from figure 13(c,d) with the curve guiding for the eyes.

in figure 10), but deviates from the experimental Δ_F^{yy} at $X_F > X_{SC}^F$. A more complicated model including multiple point forces may smear out the shallow negative Δ_F^{yy} derived from our model with single Stokeslet approximation. Nevertheless, the agreement between the experimental and theoretical results in figure 10 ensures the validity and efficiency of this simple analytical model to describe the strongly screened HIs of ellipsoids in channel confinement.

Here, Δ_F^{xx} , Δ_F^{yy} and Δ_F^{xy} decay to zero at $X_{SC}^F/R \approx 1.5$, 0.5 and 0.8, respectively, for various p and w (vertical dashed lines in figure 10). Here X_{SC}^F is the screening length of $\Delta_F^{\mu\nu}$. These different values of X_{SC}^F/R indicate that the channel confinement suppresses the transverse local flow more than the axial flow. It explains the experimental phenomena in figure 4 that the screening length X_{SC} is shortest for R–R coupling, intermediate for T–R coupling and longest for T–T coupling of two ellipsoids.

The fittings in figures 10 and 11 show that the cylinder radius R is sensitive to w and Y/w but not to p , while the dumbbell length X_{OF} is sensitive to p but not to w and Y/w . The effects of channel confinement, i.e. w and Y/w and particle anisotropy, i.e. p , on HIs are captured separately and quantitatively by the cylinder radius R and the dumbbell length X_{OF} in our theoretical model. Figure 11(a) shows that R increases with w and linearly decreases as Y/w increased. It reflects the stronger geometric confinement for particles closer to the channel wall can be linearly characterized by the smaller R . This results in that R/w decreases and Y/R increases with Y/w (see figure 11b,c), respectively. Here R/w or Y/R show different trends as a function of Y/w for channels with different cross-section shapes (figure 11b,c). Here, we discover that the fitted cylinder radius R is sensitive to both the degree of channel confinement (w , Y/w) and the channel geometry (w/d). As illustrated in figure 11(d), X_{OF}/a increases with p and becomes asymptotic to 1 at large p , indicating that the effective point forces move toward the ellipsoid tips as the ellipsoid shape becomes more anisotropic. It predicts the increase of screening length $X_{SC} = X_{SC}^F + 2X_{OF}$ with a and p (see figure 4a). At small p , the logarithmic extrapolation of X_{OF}/a in figure 11(d) correctly yields $X_{OF}/a = 0$ at $p = 1$ for spheres (Cui *et al.* 2002, 2004; Valley *et al.* 2007; Diamant 2009; Novikov *et al.* 2010), reflecting the accuracy of the dumbbell model. As a result, $X_{SC} = X_{SC}^F$ for D_C^{xx} of spheres in q1D groove channels (Cui *et al.* 2002) is much shorter than X_{SC} for ellipsoids.

This model also explains the change in coupling strength at different parameter regimes in figures 2, 3 and 5. The more enhanced T–T coupling for ellipsoids of larger p (see figures 2a–d and 5a–d) arises from the larger Δ_F^{xx} for closer point-force pair, i.e. at

shorter $X_F = X - 2X_{OF}$ due to longer X_{OF} (see figure 11d). The weak θ – θ coupling for ellipsoids with $p \leq 2.2$ (see figures 2e–h and 5e–h) can be attributed to that the moment arm $X_{OF}/a < 0.5$ is too small for slightly anisotropic particles to induce sufficient torque against thermal fluctuations. The θ – θ coupling decreases at $p \geq 5.2$ in figures 2e–h and 5e–h can be regarded as a result of the accumulation of negative Δ_F^{yy} (see figures 9b and 10e–h) along the surface of largely anisotropic ellipsoids. The strongest T–R coupling at middle Y/w (see figures 2i–l, 3i–l and 5i–l) is consistent with the maximum Δ_F^{xy} at middle Y/R (see figures 9c and 10i–l).

5. Numerical simulation

5.1. Comparisons between the simulation, experimental and theoretical results

We further perform three-dimensional finite element numerical simulations to verify the theoretical model by comparing the experimental, simulation and theoretical results, and to interpret the experimental HIs by calculating the flow field. The finite element numerical simulations are carried out using the software Comsol Multiphysics v5.2. To connect between the experimental system and theoretical model in the simulation, we use the geometries of two ellipsoids in an effective cylinder in the theoretical model, and input the parameters of the size (a , b) and axial and angular velocities (u , ω) of the ellipsoids, and the fitted radius R of the cylinder for the groove channels with width w in the experiment. The two ellipsoids are separated with (X, Y) and symmetrically located about the central axis of the cylinder. We set no-slip boundary conditions on the surface of the ellipsoids and cylinder, and open boundary conditions at the two ends of the cylinder.

In order to simplify the calculation, we apply an instantaneous axial velocity $u = (u_1 = \Delta x_1/\Delta t, u_2 = 0)$ or an instantaneous angular velocity $\omega = (\omega_1 = \Delta\theta_1/\Delta t, \omega_2 = 0)$ separately on the ellipsoid pair at each (X, Y) in a cylindrical channel with radius R (see figure 8), i.e. let one ellipsoid move and the other be at rest. We set the typical velocities ($u_1 = 1 \mu\text{m s}^{-1}$, $\omega_1 = 2^\circ \text{s}^{-1}$) and $\Delta t = 0.1 \text{ s}$ according to the ellipsoid motions and frame rate in the experiment. We solve the Stokes equation in the cylinder and yield \mathbf{F} and \mathbf{L} from integrating the force distribution density over the ellipsoid surface. Thus each component term of $\boldsymbol{\zeta}$ is directly calculated through (1.3), and the matrix of diffusion tensors \mathbf{D} at each (X, Y) is obtained through (1.2) (Montgomery & Berne 1977; Mazo 2002). Due to the velocity-independency of $\boldsymbol{\zeta}$, a different set of velocity and Δt will not change the results as long as (i) the Reynolds number is approximately 10^{-6} for micron-sized particles and (ii) $x_1(0) - 0.1a < x_1(\Delta t) < x_1(0) + 0.1a$ for ellipsoid 1. Here $0.1a$ is the bin size in the analysis of experimental results. Such a numerical method in the Comsol software has been used in the study of HIs of two spheres in a cylindrical channel in Misiunas *et al.* (2015). More benchmarking studies for the numerical method can be found in Dettmer *et al.* (2014), Misiunas *et al.* (2015) and Misiunas & Keyser (2019). The numerical simulation results of hydrodynamic coupling diffusivities $D_C^{xx}(X)$, $D_C^{x\theta}(X)$ and $D_C^{\theta\theta}(X)$ for an ellipsoid pair in the effective cylinder are shown in figure 12, which reproduce the experimental results for the coaxial and most off-axis ellipsoid pairs in the groove channels in figure 2. The screening lengths X_{SC} in the effective cylinder obtained in simulation (see figure 13) are consistent with those in the groove channels measured in experiments (see figure 5). Applying velocities in opposite directions gives the same quantitative results. The agreement between the experimental and simulation results confirm the validity of using the tube model to mimic the groove-like channel for the in-plane motions.

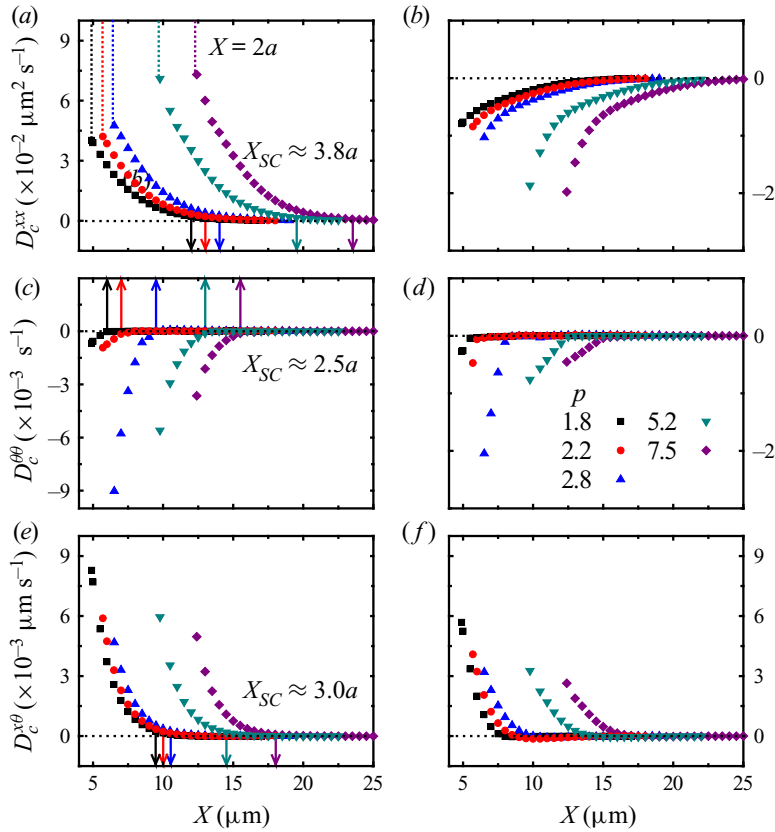


Figure 12. Numerical simulation results of coupling diffusivities $D_C(X)$. (a,c,e) The coaxial (cylindrical radius $R=9.8\ \mu\text{m}$ corresponding to $Y/w \in [0, 0.1)$ and $w=6\ \mu\text{m}$ in experiments) and (b,d,f) the off-axis ($R=6.5\ \mu\text{m}$, $Y/w \in [0.5, 0.7)$ and $w=6\ \mu\text{m}$) ellipsoid pairs with different p . The vertical arrows mark the screening length X_{SC} . Here D_C is calculated from the simulation result of ζ based on (1.2) in order to compare with the experimental D_C in figure 2.

We further transform the numerical simulation results of D_C into $\Delta_F^{\mu\nu}$ and quantitatively compare them with the theoretical prediction by fitting the dumbbell length $2X_{OF}$. Figure 14 shows that both the simulation and experimental results of Δ_F^{xx} , Δ_F^{yy} and Δ_F^{xy} coincide with their theoretical curves. The fitted X_{OF} at each p from the simulation are the same in the three curves and consistent with those fitted from the experiment with only a 3%–5% systematic exceedance (see figure 11d). This exceedance probably reflects the larger hydrodynamic diameter than the geometrical diameter, which results in their effective aspect ratios slightly smaller than those used in the simulation.

5.2. Flow field induced by a moving ellipsoid in a cylinder

We measure the flow field induced by the moving ellipsoid in the numerical simulation to illustrate the effects of channel confinement and particle anisotropy on x – x , θ – θ and x – θ HIs. These flow fields in figures 15–17 are more complicated than those of colloidal spheres in strong q1D confinements (Cui *et al.* 2002; Misiunas *et al.* 2015) where the coaxial flow induced by an axially moving sphere dominated, and only a positive x – x coupling was observed. Here, we can see that the axial and rotational motion of an ellipsoid

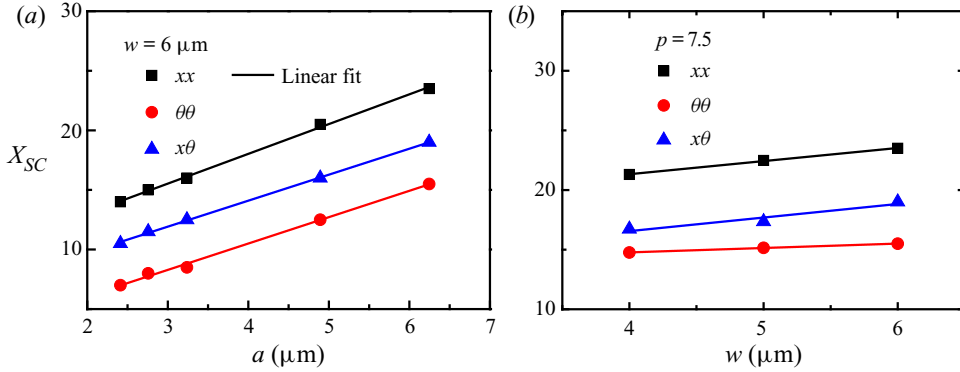


Figure 13. The numerical simulation counterpart of figure 4. The screening lengths X_{SC} (symbols) for D_C^{xx} , $D_C^{\theta\theta}$ and $D_C^{x\theta}$ of the coaxial ellipsoid pairs at $Y/w \in [0, 0.1)$. Here (a) X_{SC} for different p and $w = 6 \mu\text{m}$ and (b) X_{SC} for different w and $p = 7.5$. The lines are linear fittings.

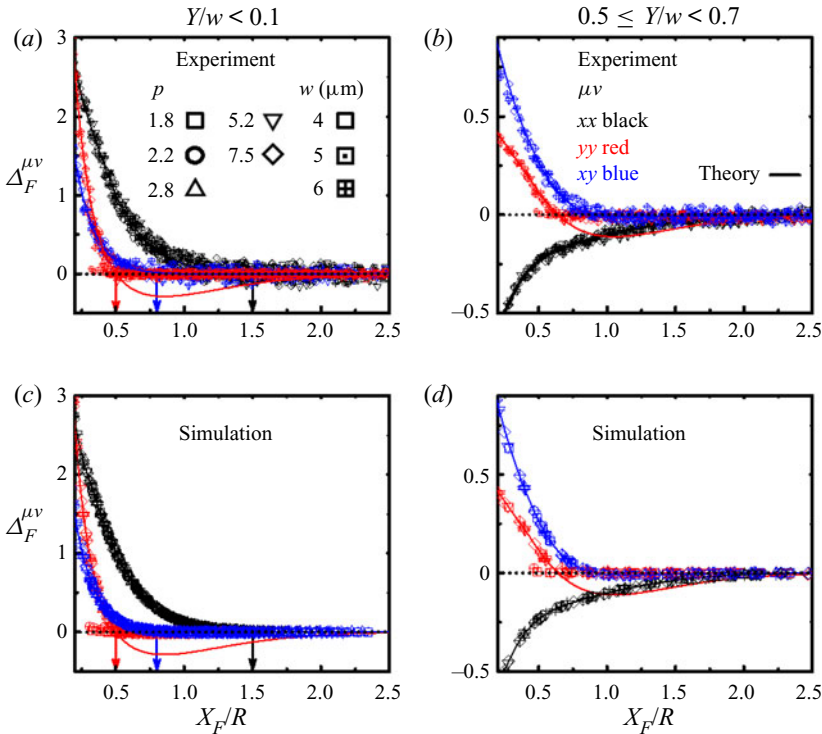


Figure 14. Rescaled coupling diffusivities $\Delta_F^{\mu\nu}(X_F/R)$. The experimental data (symbols in a,b) and the numerical simulation data (symbols in c,d) for all p and w collapse onto the theoretical curves (solid curves) of (4.2) with parameters R and X_{OF} except for the negative part of Δ_F^{yy} . (a,c) The coaxial ($Y/w \in [0, 0.1)$) and (b,d) the off-axis ($Y/w \in [0.5, 0.7)$) ellipsoid pairs. The vertical arrows mark X_{SC}^F/R .

actually reflects the axial and transverse component of the local flow field. For the coaxial ellipsoid pair in figure 15(a,c,e), a rightward axial motion of the right ellipsoid induces a rightward axial flow pulling the left ellipsoid (see figure 15a), which leads to the positive x - x coupling. The axial flow turns transversely near the ellipsoid tips causing the rotation

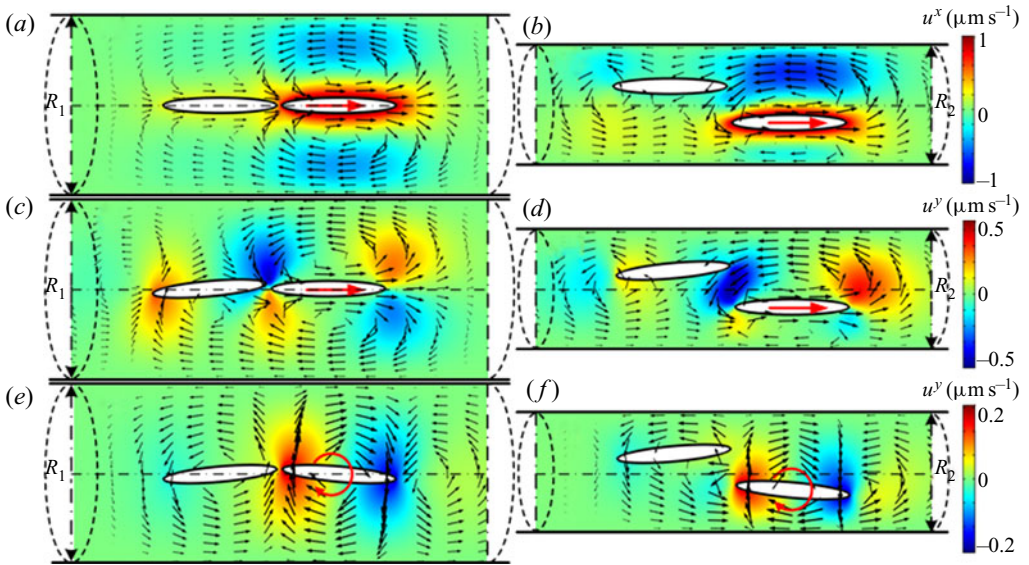


Figure 15. Numerical simulation results of the flow fields created by the motion of an ellipsoid. (a–d) Translational and (e, f) rotational motions of the right ellipsoid. (a, c, e) The coaxial (cylinder radius $R_1 = 9.8 \mu\text{m}$ corresponding to $Y/w \in [0, 0.1]$ and $w = 6 \mu\text{m}$ in experiments) and (b, d, f) the off-axis ($R_2 = 6.5 \mu\text{m}$, $Y/w \in [0.5, 0.7]$ and $w = 6 \mu\text{m}$) ellipsoid pairs with $p = 7.5$. The length and direction of the black arrows describe the local flow velocities. The colour represents the local flow speed u^v in the v direction.

of the left ellipsoid towards the axis (see figure 15c), which leads to the positive x – θ coupling. A rotation of an ellipsoid induces a whirling flow imposing a torque on the other ellipsoid in an opposite direction (see figure 15e), which leads to the negative θ – θ coupling.

By contrast, for the off-axis ellipsoid pair (see figure 15b, d, f), a rightward axial motion of the right ellipsoid induces a leftward backflow near the opposite sidewall repelling the left ellipsoid (see figure 14b), which leads to an anomalous negative x – x coupling as shown in the experiments, see figures 2(d) and 3(d). The weak channel confinement at $w/b > 4$ enables the propagation of the backflow which is necessary for the negative x – x coupling. This repulsive HI ensures the single-file motion of ellipsoids in opposite directions even in channels moderately wider than $4b$. It is in contrast to the strong q1D confinement where the piston-like motion of a sphere can only push other particles move in the same directions (Cui *et al.* 2002; Misiunas *et al.* 2015). The turning flow between the two ellipsoids' tips in figure 15(d) is much stronger than that for the coaxial ellipsoids in figure 15(c), which results in the most enhanced x – θ coupling at middle Y/w in figures 2(i–l), 3(i–l) and 5(i–l). The whirling flow in figure 15(f) leads to similar negative θ – θ coupling as that of coaxial ellipsoids in figure 15(e). The smaller radius of the effective cylinder for more off-axis ellipsoids corresponds to stronger screening effect of the channel. As a result, the fast decay of flow field near the cylinder wall predicts weaker couplings for more off-axis ellipsoids as shown in figures 2, 3 and 5. Figure 16 shows that an ellipsoid moving in directions opposite to that in figure 15 produces similar patterns of the induced flow fields with reverse signs, which leads to the same behaviour of hydrodynamic couplings.

We further compare the flow fields of ellipsoids with different aspect ratios. Figure 17 shows that a more anisotropic ellipsoid induces a stronger flow in a larger range, which explains the longer X_{SC} and stronger HIs for larger p (see figures 2–5). Especially, the

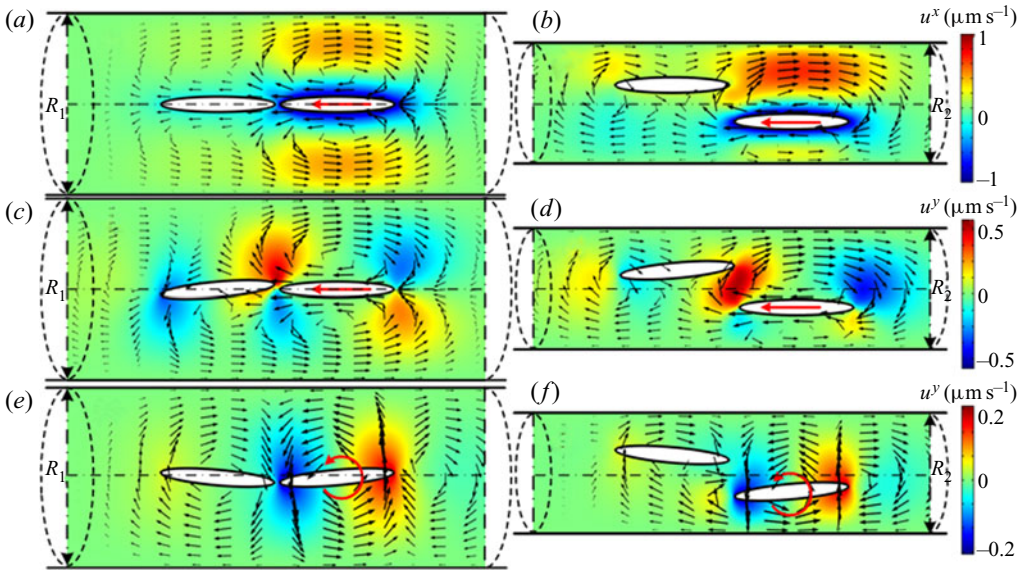


Figure 16. Simulation results of the flow fields created by the motion of an ellipsoid in the opposite direction to that in figure 15. (a–d) Translational and (e,f) rotational motions of the right ellipsoid. (a,c,e) The coaxial ($R_1 = 9.8 \mu\text{m}$ corresponding to $Y/w \in [0, 0.1]$) and $w = 6 \mu\text{m}$ in experiments) and (b,d,f) the off-axis ($R_2 = 6.5 \mu\text{m}$, $Y/w \in [0.5, 0.7]$) and $w = 6 \mu\text{m}$) ellipsoid pairs with $p = 7.5$. The length and direction of the black arrows describe the local flow velocities. The colour represents the local flow speed u^v in the v direction.

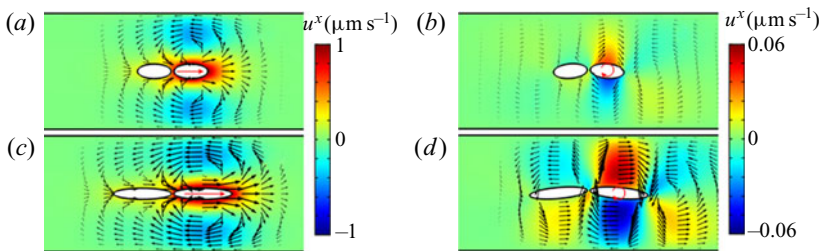


Figure 17. Numerical simulation results of the flow fields created by the motion of an ellipsoid. (a,b) Translational and (c,d) rotational motions of the right ellipsoid. The cylinder of $R = 9.8 \mu\text{m}$ corresponding to the coaxial ($Y/w \in [0, 0.1]$) ellipsoid pairs with (a,b) $p = 2.2$ and (c,d) $p = 7.5$ in a channel with $w = 6 \mu\text{m}$. The length and direction of the black arrows describe the local flow velocities. The colour represents the local flow speed u^v in the v direction.

weaker backflow at smaller p in figure 17(a,c) indicates that the backflow can be hardly probed by spheres, which may explain why the negative x – x coupling has not been observed before. The dipolar pattern of the local flow field in figures 14–16 confirms the validity of the dumbbell model for the ellipsoids. The transverse flow shows opposite directions at the two ends of an ellipsoid (see figure 15c–f). It verifies our interpretation for the suppressed transverse motion of the ellipsoids that the local flow induces mainly an effective torque rather than a transverse force. We find that the transverse flow in figure 15(e,f) decays much faster than the axial flow in figure 15(a,b), corresponding to the strongest screening of θ – θ coupling with shortest X_{SC} and the weakest screening of x – x coupling with longest X_{SC} by the channel confinement (see figures 2–5). Therefore,

the effective region of the transverse flow is relatively shorter for longer ellipsoids. This screening effect on the anisotropic particles is featured by the longer X_{OF} for larger p in the dumbbell model (see [figure 11d](#)). It results in the effective point force very close to the ellipsoid tip at $p \geq 5.2$, which leads to a slight decrease in θ – θ coupling at $p \geq 5.2$ (see [figures 2e–h](#) and [5e–h](#)).

The cylindrical tube with an appropriate diameter in our model reflects the average effects from all three walls and the open top of the groove. Particles have similar distances to the cylinder walls in the model, but a much closer distance to the bottom wall in the experiment. Such asymmetry with the lubrication flow in the bottom gap leads to a flow field distribution in the z direction different from that in the cylinder, which may make the flow field in the cylinder model quantitatively deviate from that in the experiment. Nevertheless, the HIs are still short-ranged due to the screening effect of the two sidewalls ([figures 2](#) and [3](#)) (Cui *et al.* 2002; Valley *et al.* 2007; Diamant 2009; Novikov *et al.* 2010), thus whether the top of the groove is open or closed and whether the particles are closer to the bottom wall should not qualitatively change the results when the channel is not too narrow compared with the particle size. A qualitatively different case is a very narrow tube whose diameter is close to the particle size, where T–T HI is long-ranged due to the piston flow induced by the particle (Misiunas *et al.* 2015). By contrast, for a cylinder with a radius much larger than the ellipsoid ($R \gg b$), the short-ranged swirl and back flows induced by an ellipsoid ([figures 15–17](#)) are similar to those induced by a Stokeslet (point force) in the cylinder model (Liron & Shahar 1978; Blake 1979). The open-top channels and the cylinder with comparable scale ($1 < R/w \lesssim 1.75$) have similar confinement effects on HIs in the horizontal direction for ellipsoids much smaller than the channel width ($2.99 < w/b < 7.3$ in all cases) because R/b and w/b are of the same order. The lubrication flow in the narrow bottom gap does not affect the short-range nature of the HIs in the groove because the fluid can easily flow from the sidewalls or the open top. That is, the HIs are short-ranged and the similar swirl and back flows can be qualitatively expected for two ellipsoids either sediment to the bottom of an open-top channel or in the middle of a cylinder; the numerical results of two ellipsoids in a cylinder ([figures 12](#) and [13](#)) agree with the experimental results in the channel ([figures 2](#) and [4](#)); both experimental and numerical results are fitted by the model with consistent fitting parameters ([figures 10](#), [11](#) and [14](#)). Qualitatively, the decay length of flow field is comparable to w in the groove and comparable to R in the cylinder model, which is confirmed by the measured $0.8 \lesssim X_{SC}^F/w \lesssim 2$ and $0.5 \lesssim X_{SC}^F/R \lesssim 1.5$ for various p and w in [figures 11](#) and [12](#). Therefore, the cylinder model with the Stokeslet approximation can capture the main features of the experimental T–T, T–R and R–R couplings ([figures 10](#) and [11](#)). Such a simple analytical cylinder model has successfully captured the main features of short-ranged T–T coupling between colloidal spheres in open-top grooves (Cui *et al.* 2002; Valley *et al.* 2007; Diamant 2009; Novikov *et al.* 2010).

6. Conclusion

Our experiment, numerical simulation, and theory yield consistent results for non-trivial translational and rotational HIs in different parameter regimes of $(p, w, Y/w)$ ([figures 2–5](#), [10–14](#)). All the parameters in the experiment and the model are summarized in [table 1](#), including geometries, interparticle separations, displacements, coupling diffusivities, etc. The quantitative relations between the fitting parameters and $(p, w, Y/w)$ are shown in [figure 11](#). The particle anisotropy amplifies the range of HIs. The negative R–R and positive T–R couplings non-monotonically change with p and Y/w , respectively.

Particularly, the positive axial HI ($D_C^{xx} > 0$) under strong q1D confinements ($w/b < 4$) becomes anomalously negative ($D_C^{xx} < 0$) under weak confinements ($w/b > 4$) due to backflows in wider channels. This effect is stronger for ellipsoids with large p , which may explain its absence in previous observations of colloidal spheres. In conventional single-file diffusions, spheres are strongly confined in q1D channels and always exhibit positive axial HIs, which lead to the collective concerted motion of several neighbouring spheres (Pozrikidis 1992; Wei *et al.* 2000; Cui *et al.* 2002; Misiunas *et al.* 2015). By contrast, the negative axial HIs of ellipsoids can effectively separate ellipsoids along a channel, leading to a single-file system in wide channels. Thus, single-file diffusion is not limited to strong q1D confinement, which is previously unexpected.

These distinct HIs and diffusion behaviours of particles in different parameter regimes could involve critical implications for the migration, morphology and self-organization of particles (Raven & Marmottant 2009; Uspal, Eral & Doyle 2013) in microfluids and the two-particle microrheology (Crocker *et al.* 2000; Levine & Lubensky 2000) in confined systems (Keen *et al.* 2009). For example, the positive axial HI with $D_C^{xx} > 0$ in q1D channel ($w/b < 4$) could enhance the transport of multiple particles through channels (Misiunas *et al.* 2015), whereas the negative axial HI with $D_C^{xx} < 0$ in weak confinement ($w/b > 4$) could suppress the collective transport. Spherical particles in q1D channels exhibit interesting phonons and zigzag modes (Beatus *et al.* 2006; Fleury *et al.* 2014; Uspal & Doyle 2014). Our results suggest that these phenomena could be different and much richer for particles of different anisotropy in channels of different widths.

We find that the Stokeslet approximation is suitable not only for spherical particles (Cui *et al.* 2002) and slender bodies (Di Leonardo *et al.* 2011), but also for ellipsoids with different aspect ratios for which the configuration of Stokeslet objects depends on both the geometric confinement and the particle shape. This method can be applied to other anisotropic particles in channel confinement, which avoids the expensive computational cost with regard to the detailed surface geometries of particles and channels.

Acknowledgements. The authors thank G. Hu for the helpful discussion.

Funding. This work was supported by the National Natural Science Foundation of China (Z.Z.; grant number 11372314), (Y.W.; grant number U1738118 X.X.; grant number 11974038 and U1930402), the Strategic Priority Research Program of the Chinese Academy of Sciences (Y.W.; grant number XDB22040301); the Guangdong Basic and Applied Basic Research Foundation grant (Y.H.; grant number 2020B1515120067); and the Hong Kong Research Grants Council under the Collaborative Research Fund (Y.H.; grant number C6016–20G).

Declaration of interests. The authors report no conflict of interest.

Author ORCIDs.

 Zhongyu Zheng <https://orcid.org/0000-0003-1262-389X>;

 Xinliang Xu <https://orcid.org/0000-0003-4940-3612>;

 Yilong Han <https://orcid.org/0000-0002-1439-0121>.

Author contributions. Y.H. and Z.Z. conceived and designed the research. Z.Z. carried out the experiment, simulation and data analysis, with the help from X.X., Y.H. and Y.W. The paper was written by Z.Z. and Y.H. with the help from X.X. and Y.W. Supervision of and support for the work was carried out by Y.W. and Y.H. All authors discussed the results.

Appendix A. Theoretical expression of the dumbbell-in-cylinder model

We estimate the HI of two neighbouring ellipsoids in a channel by a dumbbell-in-cylinder model. The effect of flow field induced by the motion of an ellipsoid on the neighbouring ellipsoid is treated as equivalent to the flow field induced by the dumbbell of point

forces $(\mathbf{F}, \mathbf{F}')$. For each ellipsoid, the positions of the two point forces are (x_F, y_F) and $(x_{F'}, y_{F'})$ on the long axis (see [figure 1b](#) and [table 1](#)), which are symmetric around the ellipsoid's CM at (x, y) . Because $\Delta\theta$ is small in the narrow channel, $\Delta y_{F1} = \Delta\theta_1 \times X_{OF}$ for the left ellipsoid and $\Delta y_{F2} = -\Delta\theta_2 \times X_{OF}$ for the right ellipsoid in [figure 8](#), representing that the rotational motion of the ellipsoid is dominated by the transverse displacement of point (x_F, y_F) . Hence, the axial translational motion $\Delta x = \Delta x_F = \Delta x_{F'}$ and the rotational motion $\Delta y_F = -\Delta y_{F'}$ are proportional to the axial force $F^x = F'^x$ and transverse force $F^y = -F'^y$, respectively. This dumbbell-in-cylinder model for ellipsoids in channel is a generalization of the point-force approximation for colloidal spheres in Cui *et al.* (2002) and Novikov *et al.* (2010). The point-force approximation was used to describe the translational coupling of spheres, and our dumbbell-in-cylinder model enables representation of the translational, rotational and cross-couplings, as described subsequently. According to Appendix B of Liron & Shahar (1978), the dimensionless hydrodynamic coupling tensor for a point force in a cylinder

$$\Delta_F^{\mu\nu} \equiv D_{F,C}^{\mu\nu}(X_F/R, Y_F/R)/(k_B T/6\pi\eta R) = \langle \Delta\mu_{F1} \Delta\nu_{F2} \rangle / (2tk_B T/6\pi\eta R) = 6\pi\eta R G^{\mu\nu}, \quad (\text{A1})$$

with μ and ν denoting either x or y component. Here, the Stokes-flow Oseen tensor in the cylinder

$$G^{\mu\nu} = u^{\mu\nu}/(\eta R), \quad (\text{A2})$$

where η is the viscosity and R is the radius of the cylinder. By substituting (A2) into (A1), we obtain the dimensionless coupling diffusivity

$$\Delta_F^{\mu\nu} = 6\pi u^{\mu\nu}. \quad (\text{A3})$$

The dimensionless $u^{\mu\nu}(x_{F1} = 0, y_{F1} = y_1, x_{F2} = X_F, y_{F2} = y_2)$ is the fluid velocity at (x_{F2}, y_{F2}) in the μ direction induced by a unit point force at (x_{F1}, y_{F1}) pointing to the ν direction (Liron & Shahar 1978; Blake 1979):

$$\left\{ \begin{aligned} u^{xx}(\xi^X, \xi^{y_1}, \xi^{y_2}) &= \sum_{k=-\infty}^{\infty} \left\{ -2\pi \sum_{n=1}^{\infty} e^{-\beta_{kn}\xi^x} \text{Im}[e^{i\alpha_{kn}\xi^x} F_{1,kn}^{xx}(\xi^{y_1}, \xi^{y_2})] \right. \\ &\quad \left. - \pi \sum_{n=1}^{\infty} e^{-\gamma_{kn}\xi^x} \text{Im}[F_{2,kn}^{xx}(\xi^{y_1}, \xi^{y_2})] \right\}, \\ u^{yy}(\xi^X, \xi^{y_1}, \xi^{y_2}) &= \sum_{k=-\infty}^{\infty} \left\{ -2\pi \sum_{n=1}^{\infty} e^{-\beta_{kn}\xi^x} \text{Im}[e^{i\alpha_{kn}\xi^x} F_{1,kn}^{yy}(\xi^{y_1}, \xi^{y_2})] \right. \\ &\quad \left. - \pi \sum_{n=1}^{\infty} e^{-\gamma_{kn}\xi^x} \text{Im}[F_{2,kn}^{yy}(\xi^{y_1}, \xi^{y_2})] \right\}, \\ u^{xy}(\xi^X, \xi^{y_1}, \xi^{y_2}) &= \sum_{k=-\infty}^{\infty} \left\{ 2\pi \sum_{n=1}^{\infty} e^{-\beta_{kn}\xi^x} \text{Re}[e^{i\alpha_{kn}\xi^x} F_{1,kn}^{xy}(\xi^{y_1}, \xi^{y_2})] \right. \\ &\quad \left. + \pi \sum_{n=1}^{\infty} e^{-\gamma_{kn}\xi^x} \text{Re}[F_{2,kn}^{xy}(\xi^{y_1}, \xi^{y_2})] \right\}. \end{aligned} \right. \quad (\text{A4})$$

Here, $\xi^X = |x_2 - x_1|/R = X_F/R$, $\xi^{y_1} = y_1/R$ and $\xi^{y_2} = y_2/R$. Here Im and Re denote the imaginary and real parts of a complex number, respectively. Here also

$$\left\{ \begin{aligned} F_{j,kn}^{xx}(\xi^{y_1}, \xi^{y_2}) &= \frac{\psi^x(s_{kn}^j, k, \xi^{y_1}) I_k(s_{kn}^j \xi^{y_2}) + [s_{kn}^j \xi^{y_2} I'_k(s_{kn}^j \xi^{y_2}) + I_k(s_{kn}^j \xi^{y_2})] \pi^x(s_{kn}^j, k, \xi^{y_1})}{D'_k(s_{kn}^j)}, \\ F_{j,kn}^{yy}(\xi^{y_1}, \xi^{y_2}) &= \left\{ \frac{\psi^y(s_{kn}^j, k, \xi^{y_1}) I'_k(s_{kn}^j \xi^{y_2}) + \varpi^y(s_{kn}^j, k, \xi^{y_1}) k I_k(s_{kn}^j \xi^{y_2})}{(s_{kn}^j \xi^{y_2}) + \pi^y(s_{kn}^j, k, \xi^{y_1}) s_{kn}^j \xi^{y_2} I''_k(s_{kn}^j \xi^{y_2})} \right\} / D'_k(s_{kn}^j), \\ F_{j,kn}^{xy}(\xi^{y_1}, \xi^{y_2}) &= - \frac{\psi^y(s_{kn}^j, k, \xi^{y_1}) I_k(s_{kn}^j \xi^{y_2}) + [s_{kn}^j \xi^{y_2} I'_k(s_{kn}^j \xi^{y_2}) + I_k(s_{kn}^j \xi^{y_2})] \pi^y(s_{kn}^j, k, \xi^{y_1})}{D'_k(s_{kn}^j)}, \end{aligned} \right. \quad (\text{A5})$$

where I_k is the k th-order modified Bessel function of the first kind. Here $s_{kn}^{j=1} = \alpha_{kn} + i\beta_{kn}$ and $s_{kn}^{j=2} = i\gamma_{kn}$ are two independent roots of $D_k(s) = sI_k(s)(I_{k-1}(s)I_{k+1}(s))' - 2(sI_k(s))'I_{k-1}(s)I_{k+1}(s) = 0$. The detailed functions of $\psi(s, k, \xi^{y_1})$, $\varpi(s, k, \xi^{y_1})$ and $\pi(s, k, \xi^{y_1})$ are given in Liron & Shahar (1978). By substituting (A5) into (A4), we obtain

$$\left\{ \begin{aligned} u^{xx}(\xi^X, \xi^{y_1}, \xi^{y_2}) &= \sum_{k=-\infty}^{\infty} \left\{ 2\pi \sum_{n=1}^{\infty} [a_{kn}^{xx}(\xi^{y_1}, \xi^{y_2}) \cos(\alpha_{kn} \xi^X) \right. \\ &\quad \left. + b_{kn}^{xx}(\xi^{y_1}, \xi^{y_2}) \sin(\alpha_{kn} \xi^X)] e^{-\beta_{kn} \xi^X} + \pi \sum_{n=1}^{\infty} c_{kn}^{xx}(\xi^{y_1}, \xi^{y_2}) e^{-\gamma_{kn} \xi^X} \right\}, \\ u^{yy}(\xi^X, \xi^{y_1}, \xi^{y_2}) &= \sum_{k=-\infty}^{\infty} \left\{ 2\pi \sum_{n=1}^{\infty} [a_{kn}^{yy}(\xi^{y_1}, \xi^{y_2}) \cos(\alpha_{kn} \xi^X) \right. \\ &\quad \left. + b_{kn}^{yy}(\xi^{y_1}, \xi^{y_2}) \sin(\alpha_{kn} \xi^X)] e^{-\beta_{kn} \xi^X} + \pi \sum_{n=1}^{\infty} c_{kn}^{yy}(\xi^{y_1}, \xi^{y_2}) e^{-\gamma_{kn} \xi^X} \right\}, \\ u^{xy}(\xi^X, \xi^{y_1}, \xi^{y_2}) &= \sum_{k=-\infty}^{\infty} \left\{ 2\pi \sum_{n=1}^{\infty} [a_{kn}^{xy}(\xi^{y_1}, \xi^{y_2}) \cos(\alpha_{kn} \xi^X) \right. \\ &\quad \left. + b_{kn}^{xy}(\xi^{y_1}, \xi^{y_2}) \sin(\alpha_{kn} \xi^X)] e^{-\beta_{kn} \xi^X} + \pi \sum_{n=1}^{\infty} c_{kn}^{xy}(\xi^{y_1}, \xi^{y_2}) e^{-\gamma_{kn} \xi^X} \right\}. \end{aligned} \right. \quad (\text{A6})$$

Here, the values of the parameters α_{kn} , β_{kn} and γ_{kn} are available in Liron & Shahar (1978). Here $a_{kn}^{\mu\nu}(\xi^{y_1}, \xi^{y_2}) = -\text{Im}[F_{1,kn}^{\mu\nu}(\xi^{y_1}, \xi^{y_2})]$, $b_{kn}^{\mu\nu}(\xi^{y_1}, \xi^{y_2}) = -\text{Re}[F_{1,kn}^{\mu\nu}(\xi^{y_1}, \xi^{y_2})]$ and $c_{kn}^{\mu\nu}(\xi^{y_1}, \xi^{y_2}) = -\text{Im}[F_{2,kn}^{\mu\nu}(\xi^{y_1}, \xi^{y_2})]$ for $\mu = \nu$, and $a_{kn}^{\mu\nu}(\xi^{y_1}, \xi^{y_2}) = \text{Re}[F_{1,kn}^{\mu\nu}(\xi^{y_1}, \xi^{y_2})]$, $b_{kn}^{\mu\nu}(\xi^{y_1}, \xi^{y_2}) = \text{Im}[F_{1,kn}^{\mu\nu}(\xi^{y_1}, \xi^{y_2})]$ and $c_{kn}^{\mu\nu}(\xi^{y_1}, \xi^{y_2}) = \text{Re}[F_{2,kn}^{\mu\nu}(\xi^{y_1}, \xi^{y_2})]$ for $\mu \neq \nu$.

In our experiments, $y_1 = -y_2$, as shown in § 3.2, that is, $\xi^{y1} = -\xi^{y2}$. By substituting (A6) into (A3) and taking $(\xi^{y1} = -\xi^Y/2, \xi^{y2} = \xi^Y/2)$, we obtain (4.2) in § 4.1 of the main text. We find that the experimental data of $\Delta_F^{\mu\nu}(\xi^X = (X - 2X_{OF})/R, \xi^Y = Y/R) = 6\pi\mu^{\mu\nu}(\xi^X, \xi^Y)$ is well-described theoretically by taking $k = 0, 1, 2, 3$ and $n = 1, 2, 3$ in (A6) (see figures 9 and 10). Here X_{OF} and R are obtained by fitting the three types of couplings: Δ_F^{xx} , Δ_F^{yy} and Δ_F^{xy} . Note that Δ_F^{yy} mainly characterizes the θ – θ coupling, while D_C^{yy} characterizes the y – y coupling.

To compare the simulation results of hydrodynamic couplings with the theoretical model, we fit the simulation results of the rescaled dimensionless coupling diffusivities (Liron & Shahar 1978; Cui *et al.* 2002) $\Delta_F^{\mu\nu} \equiv D_{F,C}^{\mu\nu}(X_F/R = (X - 2X_{OF})/R, Y_F/R = Y/R)/(k_B T/6\pi\eta R)$ with the theoretical prediction and compare the fitting parameters in experiments and simulations. Here $\Delta_F^{\mu\nu}$ is calculated by transforming the hydrodynamic couplings D_C of ellipsoids in (1.2) to $D_{F,C}^{\mu\nu}$ of point forces through substituting the friction matrix (Reichert & Stark 2004)

$$\zeta_F = \begin{pmatrix} \zeta^{xx} & \zeta^{xy} \\ \zeta^{yx} & \zeta^{yy} \end{pmatrix} = \begin{pmatrix} \zeta^{xx} & \zeta^{x\theta} X_{OF}^{-1} \\ \zeta^{\theta x} X_{OF}^{-1} & \zeta^{\theta\theta} X_{OF}^{-2} \end{pmatrix} \quad (\text{A7})$$

into $D_F = k_B T \zeta_F^{-1}$ in the dumbbell-in-cylinder model. Thence, the dumbbell length $2X_{OF}$ is the only fitting parameter in the simulation, which agrees well to the experimental results in figure 11(d).

REFERENCES

- BATCHELOR, G.K. 1970 Slender-body theory for particles of arbitrary cross-section in Stokes flow. *J. Fluid Mech.* **44**, 419–440.
- BEATUS, T., TLUSTY, T. & BAR-ZIV, R. 2006 Phonons in a one-dimensional microfluidic crystal. *Nat. Phys.* **2**, 743–748.
- BERLYAND, L. & PANCHENKO, A. 2007 Strong and weak blow-up of the viscous dissipation rates for concentrated suspensions. *J. Fluid Mech.* **578**, 1–34.
- BLAKE, J.R. 1971 A note on the image system for a stokeslet in a noslip boundary. *Proc. Gamb. Phil. Soc.* **70**, 303–310.
- BLAKE, J.R. 1979 On the generation of viscous toroidal eddies in a cylinder. *J. Fluid Mech.* **95**, 209–222.
- BLEIBEL, J., DOMÍNGUEZ, A., GÜNTHER, F., HARTING, J. & OETTEL, M. 2014 Hydrodynamic interactions induce anomalous diffusion under partial confinement. *Soft Matter* **10**, 2945–2948.
- BRADY, J.F. & BOSSIS, G. 1988 Stokesian dynamics. *Annu. Rev. Fluid Mech.* **20**, 111–157.
- BRAVERMAN, L., MOWITZ, A. & WITTEN, T.A. 2020 Chiral motion in colloidal electrophoresis. *Phys. Rev. E* **101**, 062608.
- BROTTO, T., CAUSSIN, J.-B., LAUGA, E. & BARTOLO, D. 2013 Hydrodynamics of confined active fluids. *Phys. Rev. Lett.* **110**, 038101.
- BUKOWICKI, M., GRUCA, M. & EKIEL-JEŻEWSKA, M.L. 2014 Dynamics of elastic dumbbells sedimenting in a viscous fluid: oscillations and hydrodynamic repulsion. *J. Fluid Mech.* **767**, 95–108.
- CACCIUTO, A. & LUIJTEN, E. 2006 Confinement-driven translocation of a flexible polymer. *Phys. Rev. Lett.* **96**, 238104.
- CHWANG, A.T. & WU, T.Y. 1976 Hydromechanics of low-Reynolds-number flow. Part 4. Translation of spheroids. *J. Fluid Mech.* **75**, 677–689.
- CROCKER, J.C., VALENTINE, M.T., WEEKS, E.R., GISLER, T., KAPLAN, P.D., YODH, A.G. & WEITZ, D.A. 2000 Two-point microrheology of inhomogeneous soft materials. *Phys. Rev. Lett.* **85**, 888.
- CUI, B., DIAMANT, H. & LIN, B. 2002 Screened hydrodynamic interaction in a narrow channel. *Phys. Rev. Lett.* **89**, 188302.
- CUI, B., DIAMANT, H., LIN, B. & RICE, S.A. 2004 Anomalous hydrodynamic interaction in a quasi-two-dimensional suspension. *Phys. Rev. Lett.* **92**, 258301.
- DAI, L., HE, G., ZHANG, X. & ZHANG, X. 2018 Stable formations of self-propelled fish-like swimmers induced by hydrodynamic interactions. *J. R. Soc. Interface* **15**, 20180490.

- DAVIDCHACK, R.L., OULDRIDGE, T.E. & TRETYAKOV, M.V. 2017 Geometric integrator for Langevin systems with quaternion-based rotational degrees of freedom and hydrodynamic interactions. *J. Chem. Phys.* **147**, 224103.
- DETTMER, S.L., PAGLIARA, S., MISIUNAS, K. & KEYSER, U.F. 2014 Anisotropic diffusion of spherical particles in closely confining microchannels. *Phys. Rev. E* **89** (6), 062305.
- DHONT, J.K.G. 1996 *An Introduction to Dynamics of Colloids*. Elsevier, Amsterdam.
- DIAMANT, H. 2009 Hydrodynamic interaction in confined geometries. *J. Phys. Soc. Japan* **78**, 041002.
- DI LEONARDO, R., CAMMAROTA, E., BOLOGNESI, G., SCHÄFER, H. & STEINHART, M. 2011 Three-dimensional to two-dimensional crossover in the hydrodynamic interactions between micron-scale rods. *Phys. Rev. Lett.* **107**, 044501.
- DOI, M. & EDWARDS, S.F. 1988 *The Theory of Polymer Dynamics*. Oxford University Press.
- DOMÍNGUEZ, A. 2018 Theory of anomalous collective diffusion in colloidal monolayers on a spherical interface. *Phys. Rev. E* **97**, 022607.
- DRESCHER, K., DUNKEL, J., CISNEROS, L.H., GANGULY, S. & GOLDSTEIN, R.E. 2011 Fluid dynamics and noise in bacterial cell-cell and cell-surface scattering. *Proc. Natl Acad. Sci. USA* **108**, 10940–10945.
- DUFRESNE, E.R., SQUIRES, T.M., BRENNER, M.P. & GRIER, D.G. 2000 Hydrodynamic coupling of two Brownian spheres to a planar surface. *Phys. Rev. Lett.* **85**, 3317.
- DUGGAL, R. & PASQUALI, M. 2006 Dynamics of individual single-walled carbon nanotubes in water by real-time visualization. *Phys. Rev. Lett.* **96**, 246104.
- DUNKEL, J., HEIDENREICH, S., DRESCHER, K., WENSINK, H.H., BÄR, M. & GOLDSTEIN, R.E. 2013 Fluid dynamics of bacterial turbulence. *Phys. Rev. Lett.* **110**, 228102.
- DURLOFSKY, L., BRADY, J.F. & BOSSIS, G. 1987 Dynamic simulation of hydrodynamically interacting particles. *J. Fluid Mech.* **180**, 21–49.
- ERMAK, D.L. & MCCAMMON, J.A. 1978 Brownian dynamics with hydrodynamic interactions. *J. Chem. Phys.* **69**, 1352–1360.
- FLEURY, J.-B., SCHILLER, U.D., THUTUPALLI, S., GOMPPER, G. & SEEMANN, R. 2014 Mode coupling of phonons in a dense one-dimensional microfluidic crystal. *New J. Phys.* **16**, 063029.
- FOSS, D.R. & BRADY, J.F. 2000 Structure, diffusion and rheology of Brownian suspensions by Stokesian dynamics simulation. *J. Fluid Mech.* **407**, 167–200.
- GARCÍA DE LA TORRE, J., DEL RIO ECHENIQUE, G. & ORTEGA, A. 2007 Improved calculation of rotational diffusion and intrinsic viscosity of bead models for macromolecules and nanoparticles. *J. Phys. Chem. B* **111**, 955–961.
- GODDARD, B.D., NOLD, A. & KALLIADASIS, S. 2016 Dynamical density functional theory with hydrodynamic interactions in confined geometries. *J. Chem. Phys.* **145**, 214106.
- GOLDFRIEND, T., DIAMANT, H. & WITTEN, T.A. 2015 Hydrodynamic interactions between two forced objects of arbitrary shape. I. Effect on alignment. *Phys. Fluids* **27**, 123303.
- DE GRAAF, J., MENKE, H., MATHIJSEN, A.J., FABRITIUS, M., HOLM, C. & SHENDRUK, T.N. 2016 Lattice-Boltzmann hydrodynamics of anisotropic active matter. *J. Chem. Phys.* **144**, 134106.
- GRÜNBAUM, D. 1995 A model of feeding currents in encrusting bryozoans shows interference between zooids within a colony. *J. Theor. Biol.* **174**, 409–425.
- GRZYBOWSKI, B.A., STONE, H.A. & WHITESIDES, G.M. 2000 Dynamic self-assembly of magnetized, millimetre-sized objects rotating at a liquid-air interface. *Nature* **405**, 1033–1036.
- HAN, Y., ALSAYED, A., NOBILI, M. & YODH, A.G. 2009 Quasi-two-dimensional diffusion of single ellipsoids: aspect ratio and confinement effects. *Phys. Rev. E* **80**, 011403.
- HAN, Y., ALSAYED, A.M., NOBILI, M., ZHANG, J., LUBENSKY, T.C. & YODH, A.G. 2006 Brownian motion of an ellipsoid. *Science* **314**, 626–630.
- HAPPEL, J. & BRENNER, H. 1983 *Low Reynolds Number Hydrodynamics*. Kluwer Academic Publishers.
- HERNÁNDEZ-ORTIZ, J.P., DE PABLO, J.J. & GRAHAM, M.D. 2006 N log N method for hydrodynamic interactions of confined polymer systems: Brownian dynamics. *J. Chem. Phys.* **125**, 164906.
- HUANG, B., WU, H., BHAYA, D., GROSSMAN, A., GRANIER, S., KOBILKA, B.K. & ZARE, R.N. 2007 Counting low-copy number proteins in a single cell. *Science* **315**, 81–84.
- HUH, D., GU, W., KAMOTANI, Y., GROTHBERG, J.B. & TAKAYAMA, S. 2005 Microfluidics for flow cytometric analysis of cells and particles. *Physiol. Meas.* **26**, R73–R98.
- KARRILA, S.J., FUENTES, Y.O. & KIM, S. 1989 Parallel computational strategies for hydrodynamic interactions between rigid particles of arbitrary shape in a viscous fluid. *J. Rheol.* **33**, 913–947.
- KEEN, S., YAO, A., LEACH, J., DI LEONARDO, R., SAUNTER, C., LOVE, G., COOPER, J. & PADGETT, M. 2009 Multipoint viscosity measurements in microfluidic channels using optical tweezers. *Lab on a Chip* **9**, 2059–2062.
- LADD, A.J.C. 1994a Numerical simulations of particulate suspensions via a discretized Boltzmann equation. Part I. Theoretical foundation. *J. Fluid Mech.* **271**, 285–309.

- LADD, A.J.C. 1994*b* Numerical simulations of particulate suspensions via a discretized Boltzmann equation. Part 2. Numerical results. *J. Fluid Mech.* **271**, 311–339.
- LEVINE, A.J. & LUBENSKY, T.C. 2000 One-and two-particle microrheology. *Phys. Rev. Lett.* **85**, 1774.
- LIN, B., CUI, B., LEE, J.-H. & YU, J. 2002 Hydrodynamic coupling in diffusion of quasi-one-dimensional Brownian particles. *Europhys. Lett.* **57**, 724.
- LIRON, N. & SHAHAR, R. 1978 Stokes flow due to a Stokeslet in a pipe. *J. Fluid Mech.* **86**, 727–744.
- LISICKI, M., CICHOCKI, B. & WAJNRYB, E. 2016 Near-wall diffusion tensor of an axisymmetric colloidal particle. *J. Chem. Phys.* **145**, 034904.
- MARTIN, S., REICHERT, M., STARK, H. & GISLER, T. 2006 Direct observation of hydrodynamic rotation-translation coupling between two colloidal spheres. *Phys. Rev. Lett.* **97**, 248301.
- MATHIJSSSEN, A.J., DOOSTMOHAMMADI, A., YEOMANS, J.M. & SHENDRUK, T.N. 2016 Hotspots of boundary accumulation: dynamics and statistics of micro-swimmers in flowing films. *J. R. Soc. Interface* **13**, 20150936.
- MAZO, R.M. 2002 *Brownian Motion: Fluctuations, Dynamics, and Applications*. Oxford University Press.
- MAZUR, P. & VAN SAARLOOS, W. 1982 Many-sphere hydrodynamic interactions and mobilities in a suspension. *Physica A* **115**, 21–57.
- MEINERS, J.-C. & QUAKE, S.R. 1999 Direct measurement of hydrodynamic cross correlations between two particles in an external potential. *Phys. Rev. Lett.* **82**, 2211.
- MISIUNAS, K. & KEYSER, U.F. 2019 Density-dependent speed-up of particle transport in channels. *Phys. Rev. Lett.* **122** (21), 214501.
- MISIUNAS, K., PAGLIARA, S., LAUGA, E., LISTER, J.R. & KEYSER, U.F. 2015 Nondecaying hydrodynamic interactions along narrow channels. *Phys. Rev. Lett.* **115**, 038301.
- MONTGOMERY, J.A. JR. & BERNE, B.J. 1977 The effects of hydrodynamic interactions on translational and rotational relaxation. *J. Chem. Phys.* **67**, 4589–4596.
- MOWITZ, A.J. & WITTEN, T.A. 2017 Predicting tensorial electrophoretic effects in asymmetric colloids. *Phys. Rev. E* **96**, 062613.
- NOVIKOV, S., RICE, S.A., CUI, B., DIAMANT, H. & LIN, B. 2010 Hydrodynamic interactions in ribbon channels: from quasi-one-dimensional to quasi-two-dimensional behavior. *Phys. Rev. E* **82**, 031403.
- PAGÈS, J.-M., JAMES, C.E. & WINTERHALTER, M. 2008 The porin and the permeating antibiotic: a selective diffusion barrier in Gram-negative bacteria. *Nat. Rev. Microbiol.* **6**, 893–903.
- PALANISAMY, D. & DEN OTTER, W.K. 2018 Efficient Brownian Dynamics of rigid colloids in linear flow fields based on the grand mobility matrix. *J. Chem. Phys.* **148**, 194112.
- POZRIKIDIS, C. 1992 *Boundary Integral and Singularity Methods for Linearized Viscous Flow*. Cambridge University Press.
- RAVEN, J.-P. & MARMOTTANT, P. 2009 Microfluidic crystals: dynamic interplay between rearrangement waves and flow. *Phys. Rev. Lett.* **102**, 084501.
- REICHERT, M. & STARK, H. 2004 Hydrodynamic coupling of two rotating spheres trapped in harmonic potentials. *Phys. Rev. E* **69**, 031407.
- RILEY, K.F., HOBSON, M.P. & BENICE, S.J. 2006 *Mathematical Methods for Physics and Engineering: a Comprehensive Guide*. Cambridge university press.
- SOKOLOV, A., ARANSON, I.S., KESSLER, J.O. & GOLDSTEIN, R.E. 2007 Concentration dependence of the collective dynamics of swimming bacteria. *Phys. Rev. Lett.* **98**, 158102.
- SOMASI, M., KHOMAMI, B., WOO, N.J., HUR, J.S. & SHAQFEH, E.S. 2002 Brownian dynamics simulations of bead-rod and bead-spring chains: numerical algorithms and coarse-graining issues. *J. Non-Newtonian Fluid Mech.* **108**, 227–255.
- STROOCK, A.D., WECK, M., CHIU, D.T., HUCK, W.T., KENIS, P.J., ISMAGILOV, R.F. & WHITESIDES, G.M. 2000 Patterning electro-osmotic flow with patterned surface charge. *Phys. Rev. Lett.* **84**, 3314.
- TANAKA, H. 2001 Interplay between wetting and phase separation in binary fluid mixtures: roles of hydrodynamics. *J. Phys: Condens. Matter* **13**, 4637.
- TANAKA, H. 2005 Roles of hydrodynamic interactions in structure formation of soft matter: protein folding as an example. *J. Phys: Condens. Matter* **17**, S2795.
- TRAN-CONG, T. & PHAN-THIEN, N. 1989 Stokes problems of multiparticle systems: a numerical method for arbitrary flows. *Phys. Fluid A Fluid Dyn.* **1**, 453–461.
- USPAL, W.E. & DOYLE, P.S. 2014 Self-organizing microfluidic crystals. *Soft Matter* **10**, 5177–5191.
- USPAL, W.E., ERAL, H.B. & DOYLE, P.S. 2013 Engineering particle trajectories in microfluidic flows using particle shape. *Nat. Commun.* **4**, 2666.
- USTA, O.B., BUTLER, J.E. & LADD, A.J. 2007 Transverse migration of a confined polymer driven by an external force. *Phys. Rev. Lett.* **98**, 098301.

- USTA, O.B., LADD, A.J.C. & BUTLER, J.E. 2005 Lattice-Boltzmann simulations of the dynamics of polymer solutions in periodic and confined geometries. *J. Chem. Phys.* **122**, 094902.
- VALLEY, D.T., RICE, S.A., CUI, B., HO, H.M., DIAMANT, H. & LIN, B. 2007 Pair diffusion in quasi-one-and quasi-two-dimensional binary colloid suspensions. *J. Chem. Phys.* **126**, 134908.
- VILLANUEVA-VALENCIA, J.R., SANTANA-SOLANO, J., SARMIENTO-GÓMEZ, E., HERRERA-VELARDE, S., ARAUZ-LARA, J.L. & CASTAÑEDA-PRIEGO, R. 2018 Long-time dynamics and hydrodynamic correlations in quasi-two-dimensional anisotropic colloidal mixtures. *Phys. Rev. E* **98**, 062605.
- WAJNRYB, E., MIZERSKI, K.A., ZUK, P.J. & SZYMCAK, P. 2013 Generalization of the Rotne-Prager-Yamakawa mobility and shear disturbance tensors. *J. Fluid Mech.* **731**, R3.
- WEI, Q.-H., BECHINGER, C. & LEIDERER, P. 2000 Single-file diffusion of colloids in one-dimensional channels. *Science* **287**, 625–627.
- WITTEN, T.A. & DIAMANT, H. 2020 A review of shaped colloidal particles in fluids: anisotropy and chirality. [arXiv:2003.03698](https://arxiv.org/abs/2003.03698)
- WITTEN, T.A. & MOWITZ, A. 2019 Adapting the Teubner reciprocal relations for stokeslet objects. [arXiv:1907.07444](https://arxiv.org/abs/1907.07444)
- YANG, H. & KIM, S. 1995 Boundary element analysis of particle mobilities in a cylindrical channel: network-based parallel computing with condor. *Comput. Chem. Engng* **19**, 683–692.
- ZHENG, Z. & HAN, Y. 2010 Self-diffusion in two-dimensional hard ellipsoid suspensions. *J. Chem. Phys.* **133**, 124509.
- ZHENG, Z., NI, R., WANG, F., DIJKSTRA, M., WANG, Y. & HAN, Y. 2014 Structural signatures of dynamic heterogeneities in monolayers of colloidal ellipsoids. *Nat. Commun.* **5**, 3829.
- ZHENG, Z., WANG, F. & HAN, Y. 2011 Glass transitions in quasi-two-dimensional suspensions of colloidal ellipsoids. *Phys. Rev. Lett.* **107**, 065702.